On the displacement of three-dimensional fluid droplets from solid surfaces in low-Reynolds-number shear flows

By P. DIMITRAKOPOULOS and J. J. L. HIGDON

Department of Chemical Engineering, University of Illinois, Urbana, IL 61801, USA

The yield conditions for the displacement of three-dimensional fluid droplets from solid boundaries are studied through a series of numerical computations. The study considers low-Reynolds-number shear flows over plane boundaries and includes interfacial forces with constant surface tension. A comprehensive study is conducted, covering a wide range of viscosity ratio λ, capillary number Ca and advancing and receding contact angles, θ_A and θ_R. This study seeks the optimal shape of the contact line which yields the maximum flow rate (or Ca) for which a droplet can adhere to the surface. The critical shear rates are presented as functions $Ca(\lambda, \theta_A, \Delta\theta)$ where $\Delta\theta = \theta_A - \theta_R$ is the contact angle hysteresis. The solution of the optimization problem provides an upper bound for the yield condition for droplets on solid surfaces. Additional constraints based on experimental observations are considered, and their effect on the yield condition is determined. The numerical solutions are based on the spectral boundary element method, incorporating a novel implementation of Newton's method for the determination of equilibrium free surfaces and an optimization algorithm which is combined with the Newton iteration to solve the nonlinear optimization problem. The numerical results are compared with asymptotic theories (Dussan 1987) based on the lubrication approximation. While good agreement is found in the joint asymptotic limits $\Delta\theta \ll \theta_A \ll 1$, the useful range of the lubrication models proves to be extremely limited. The critical shear rate is found to be sensitive to viscosity ratio with qualitatively different results for viscous and inviscid droplets.

1. Introduction

The displacement of fluid droplets from solid substrates is a fundamental problem of fluid mechanics. Our interest in the problem focuses on drop displacement in viscous shear flows at low Reynolds number. This regime has relevance in coating operations and in enhanced oil recovery. In the coating industry, the presence of small liquid droplets or gas bubbles on solid surfaces is a major concern in the design of process equipment, because even a small flow disturbance is sufficient to destroy the uniformity required in precision film coating. In the petroleum industry, enhanced oil recovery techniques are strongly dependent on the interaction of oil and water in immiscible two-phase mixtures, and the success of such operations depends on the displacement of small oil droplets attached to solid surfaces.

The fundamental issues associated with viscous drop displacement from rigid boundaries have been addressed in a series of papers by Dussan and coworkers (Dussan & Chow 1983; Dussan 1985, 1987). These authors developed yield criteria for

the critical capillary number Ca or Bond number B_d as a function of the advancing and receding contact angles, θ_A and θ_R. In the first two articles, they considered droplets in a quiescent fluid displaced by the action of gravity. In the final article, Dussan considered the displacement of a droplet through the action of a viscous shear flow. In each of these papers, the analysis was based on asymptotic theory valid for small contact angle hysteresis $(\theta_A - \theta_R)$. Additional simplifications included the restriction to small contact angles and lubrication theory in the first and third articles and to small Bond numbers B_d in the second article. A number of authors (Feng & Basaran 1994; Li & Pozrikidis 1996) have conducted numerical studies of the droplet displacement problem. A review of these efforts as well as other asymptotic theories has been given in our recent paper (Dimitrakopoulos & Higdon 1997, hereafter referred to as DH). In that paper, we addressed the two-dimensional analogue of Dussan's problem, making no restrictions on any parameter values or flow conditions. We included gravitational effects to investigate droplets which feature large aspect ratios and relatively flat interfaces with arbitrary contact angles. An extensive study was conducted, covering a wide range of viscosity ratio λ, Bond number B_d, capillary number Ca and contact angles θ_A and θ_R. The numerical results were compared with asymptotic theories based on the lubrication approximation. While excellent agreement was found in the joint asymptotic limits $(\theta_A - \theta_R) \ll \theta_A \ll 1$, the useful range of the lubrication models proved to be extremely limited. The critical shear rate was found to be sensitive to viscosity ratio with qualitatively different results for viscous and inviscid droplets. Gravitational forces normal to the solid boundary were shown to have a significant effect on the displacement process, reducing the critical shear rate for viscous drops and increasing the rate for inviscid droplets. The low-viscosity limit $\lambda \to 0$ was shown to be a singular limit in the lubrication theory, and the proper scaling for Ca at small λ was identified.

In the present article, we focus our attention on the displacement of a three-dimensional fluid droplet from a plane substrate due to the action of a viscous shear flow. Our goal is to provide a comprehensive solution of the problem, and hence to assess the limits of the asymptotic theories and to determine the effects of the viscosity ratio. We consider arbitrary values for the contact angles, the contact angle hysteresis $(\theta_A - \theta_R)$ and the viscosity ratio λ. We seek the optimal shape of the contact line C which provides the maximum flow rate (or Ca) for which a droplet can adhere to the surface. This critical Ca constitutes the yield condition and is expressed as a function of contact angle θ_A, hysteresis $(\theta_A - \theta_R)$ and viscosity ratio λ. In this effort, we determine the equilibrium shapes of the fluid interface. As in the previous paper, we define an *equilibrium* shape to be a stationary interface for which all kinematic and dynamic boundary conditions are satisfied under conditions of steady flow. This should not be confused with the concept of equilibrium surfaces under quiescent conditions.

To address these problems, we employ the spectral boundary element method described by Occhialini, Muldowney & Higdon (1992) and further discussed by Muldowney & Higdon (1995). This algorithm is combined with an iterative scheme to determine the equilibrium shapes of the fluid interface. In prior boundary element studies, most authors have determined equilibrium shapes by time-dependent computations (e.g. Li & Pozrikidis 1996) or simple iterative strategies with slow convergence rates over small domains (see Pozrikidis 1992). Here we employ a novel approach which implements a Newton iteration scheme within the boundary integral framework. This method is the three-dimensional analogue of the two-dimensional Newton iteration presented in DH. We obtain the rapid convergence characteristic of Newton's
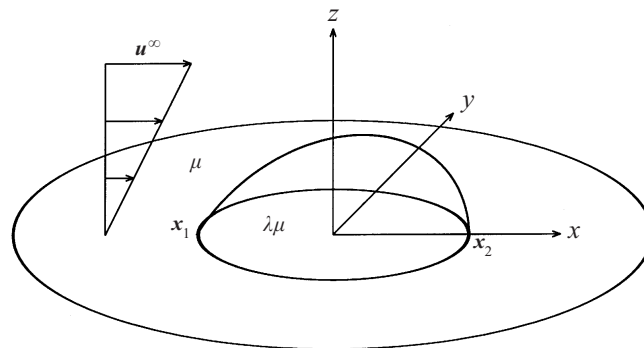
FIGURE 1. Fluid droplet attached to a solid boundary in a viscous shear flow.

method and find a large radius of convergence. The performance of this algorithm compares well with the Newton iteration method of Higdon & Schnepper (1994), but the implementation is simpler than that of the earlier procedure.

In the analysis of free-surface flows, Newton's method has long been established as an effective tool in the finite element literature. The implementation of these algorithms has been discussed in numerous publications by Scriven and coworkers with application to coating flows. Early efforts employing algebraic grid generation are discussed by Saito & Scriven (1981) and by Kistler & Scriven (1984*a,b*), while more recent implementations based on elliptic mesh generation are described by Christodoulou & Scriven (1992). Additional references for finite element/Newton's method applications in free surface flow are cited in these publications, as well as in the aforementioned work of Feng & Basaran (1994). In the implementation of a Newton method for boundary integral computations, we seek to extend to this class of algorithms an effective technique which has long proved its value in the field of finite element computations.

2. Mathematical formulation

We consider a three-dimensional droplet attached to a plane solid boundary as illustrated in figure 1. The droplet size is specified by its volume V_0 or equivalently by the radius a of a spherical droplet of volume $V_0 = (4\pi/3)a^3$. The droplet (fluid 1) has density ρ_1 and viscosity $\lambda\mu$, while the surrounding fluid has density ρ_2 and viscosity μ. The gravitational acceleration is g and the gravity vector forms an angle β with respect to the negative z-direction; hence β is the angle of inclination of the plane substrate.† The surface tension γ is assumed constant. The undisturbed flow exterior to the droplet is that of a simple shear flow $u^\infty = (Gz, 0, 0)$ where G is the shear rate. The contact line forms a closed curve C in the (x, y)-plane which intersects the x-axis at two points, with the upstream point and contact angle designated x_1 and θ_1, and the corresponding downstream ones x_2 and θ_2.

The capillary number Ca and Bond number B_d are defined by

$$Ca = \frac{\mu Ga}{\gamma}, \qquad B_d = \frac{(\rho_1 - \rho_2)ga^2}{\gamma}.$$

† While we do not include gravity effects in the present paper, we include the body force for future reference and to maintain a general formulation.

The governing equations in the infinite fluid are the Stokes equations together with continuity

$$\nabla \cdot \boldsymbol{\sigma} = -\nabla p + \mu \nabla^2 \boldsymbol{u} = 0, \tag{1}$$

$$\nabla \cdot \boldsymbol{u} = 0, \tag{2}$$

with similar expressions for the droplet, with the viscosity replaced by $\lambda\mu$.

The boundary conditions on the solid wall and at infinity give

$$\boldsymbol{u} = 0 \quad \text{on} \quad z = 0, \tag{3}$$

$$\boldsymbol{u} \to \boldsymbol{u}^{\infty} \quad \text{as} \quad r \to \infty. \tag{4}$$

At the interface, the boundary conditions on the velocity $\boldsymbol{u}$ and surface stress $\boldsymbol{f}$ are

$$\boldsymbol{u}_1 = \boldsymbol{u}_2, \tag{5}$$

$$\Delta \boldsymbol{f} = \boldsymbol{f}_2 - \boldsymbol{f}_1 = \gamma(\nabla \cdot \boldsymbol{n})\boldsymbol{n} + (\rho_2 - \rho_1)(\boldsymbol{g} \cdot \boldsymbol{x})\boldsymbol{n}. \tag{6}$$

Here the subscripts designate quantities evaluated in fluids 1 and 2 respectively. The surface stress is defined as $\boldsymbol{f} = \boldsymbol{\sigma} \cdot \boldsymbol{n}$, and $\boldsymbol{n}$ is the unit normal which we choose to point into fluid 2. The pressure as defined in $\boldsymbol{\sigma}$ is the dynamic pressure, hence the gravity force is absent from (1) and appears in the interfacial stress boundary condition (6).

With an interface of prescribed shape, the equations and boundary conditions (1)–(6) constitute a well-posed boundary value problem from which one may determine the velocity and stress throughout both fluid regions. For a droplet surface of arbitrary shape, the solution for the flow field will not in general correspond to a stationary equilibrium shape. For *equilibrium shapes*, the velocity field must satisfy an additional constraint – the kinematic condition at the interface

$$\boldsymbol{u}_1 \cdot \boldsymbol{n} = \boldsymbol{u}_2 \cdot \boldsymbol{n} = 0. \tag{7}$$

Although the governing equations and boundary conditions are linear in $\boldsymbol{u}$ and $\boldsymbol{f}$, the problem of determining equilibrium droplet shapes constitutes a nonlinear problem for the unknown interface Γ: that is the velocity $\boldsymbol{u}$ and stress $\boldsymbol{f}$, as well as the curvature $\nabla \cdot \boldsymbol{n}$ are nonlinear functions of the geometrical variables describing the interface shape. For a given flow field $\boldsymbol{u}^{\infty}$ and droplet volume $V_0 \equiv (4\pi/3)a^3$, there is no guarantee that an equilibrium shape exists, nor is there any certainty that such solutions are unique.

For freely suspended droplets, the system of equations (1)–(7) is sufficient to determine the family of equilibrium surfaces. For droplets in contact with a solid boundary, additional conditions are required to prescribe the interface shape in the vicinity of the contact line. The boundary conditions at the contact line relate the contact angle θ to the position and velocity of the contact line. A wealth of literature has been devoted to this subject with a review of early work given by Dussan (1979), and a comprehensive review of more recent work given by Kistler (1993). We note that the prediction of dynamic contact angles for moving contact lines poses a far greater challenge than that for the static contact angles required in the present study. We refer the reader to Chen, Rame & Garoff (1995) for further discussion of recent work in this area.

For a stationary contact line, the boundary condition is determined by the nature of the solid surface. For a rough surface, one may require that the contact line remains at fixed position while allowing the contact angle to vary over a wide range. This is the condition assumed by Feng & Basaran (1994) and Li & Pozrikidis (1996). From an experimental viewpoint, this condition may be realized by a droplet attached to an

orifice or a slit in the plane (Feng & Basaran 1994; Oliver, Huh & Mason 1977). At the opposite extreme, one may consider a perfectly smooth, homogeneous surface on which the contact angle takes a single value θ. An elementary force balance (Dussan & Chow 1983; DH) shows that a droplet on a such a surface cannot resist a net force arising from fluid motion; hence such stationary droplets could exist only in quiescent fluids. For real surfaces, it has been found that the static contact angle exhibits a hysteresis effect where the contact line remains stationary for any angle in the range $\theta_R \leqslant \theta \leqslant \theta_A$. The limits θ_A and θ_R are called the advancing and receding angles respectively. There is an extensive literature on the phenomenon of contact angle hysteresis, and a brief review has been given in our recent paper on drop displacement (DH).

In the present work, we have chosen to model the contact line using the formalism of contact angle hysteresis. We assume that the advancing and receding angles θ_A and θ_R are physical constants and require that $\theta_R \leqslant \theta \leqslant \theta_A$ for all angles along the contact line C. To implement the boundary conditions at the contact line, we proceed in two distinct steps. In the first step, we develop an algorithm for a contact line of prescribed shape C_0. For this contact line, and a specified capillary number Ca, we determine the equilibrium droplet shape Γ and the resulting distribution of contact angles θ. In the second step, we implement an optimization algorithm, and search among all possible curves C to find that contact curve which minimizes the contact angle hysteresis $\theta_A - \theta_R$ for a specified θ_A and Ca. The results of this search give the yield condition for the drop displacement process in terms of well-defined physical parameters. In the solution procedure, we solve for $\theta_A - \theta_R$ as a function of Ca; however, the final results may equally be viewed as $Ca(\theta_A - \theta_R)$. In this form, our results address the simple physical question: for given contact angles θ_A and θ_R, what flow rate or Ca is required to dislodge the droplet from the surface; i.e. what is the highest Ca for which an equilibrium solution exists at the specified $\theta_A - \theta_R$. Details regarding the solution of the optimization problem are given in the section below.

2.1. *Boundary integral formulation*

The fundamental solution for the three-dimensional Stokes equations is designated S_{ij} and the associated stress is T_{ijk}. These solutions may be written in the form

$$S_{ij} = \frac{\delta_{ij}}{r} + \frac{\hat{x}_i \hat{x}_j}{r^3}, \tag{8}$$

$$T_{ijk} = -6 \frac{\hat{x}_i \hat{x}_j \hat{x}_k}{r^5}, \tag{9}$$

where $\hat{x} = x - x_0$ and $r = |\hat{x}|$.

By introducing the fundamental solution and integrating over a volume of fluid bounded by a surface S, the velocity at a point x_0 on the surface is expressed

$$u(x_0) = -\frac{1}{4\pi\mu} \int_S [S \cdot f - \mu T \cdot u \cdot n] \, dS. \tag{10}$$

The derivation of this integral formula is presented in standard references, see Pozrikidis (1992). Here we have chosen the unit normal vector pointing into the volume of fluid.

For a fluid droplet attached to a solid surface, one may model the effect of the solid in two ways. In the first, one employs the Green's function for a half-space bounded by a solid plane (Pozrikidis 1992), and the surface of integration in (10) reduces to that of the fluid–fluid interface. In the second approach, one employs the free-space
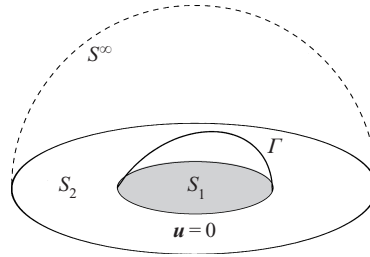
FIGURE 2. Domain geometry for boundary integral solution for viscous flow past a droplet attached to a solid boundary.

Green's function (8), and the solid boundary becomes part of the boundary surface S. In the numerical solution, the first approach leads to fewer unknowns, while the second approach leads to simpler programming effort and numerical integration. In addition, the second approach is readily extended to solid boundaries of more general shape. Either method is quite effective for the present problem, and we have chosen the second approach with the boundary surfaces as shown in figure 2.

To develop the integral formula for our problem, we consider a large hemispherical domain bounded by the solid plane and a hemisphere S^∞ of large radius. For the flow exterior to the droplet, we define the disturbance velocity $u_2^D = u_2 - u^\infty$ and write an equation of the form (10) in terms of this velocity and its associated stress. In the limit as the radius of S^∞ approaches infinity, the integral on S^∞ vanishes. The remaining surfaces are the solid plane and the interface Γ separating the two fluids. The portion of the boundary wall in contact with fluid 1 is designated S_1, while the remaining portion in contact with fluid 2 is designated S_2. The boundary condition on the outer portion of the plane wall S_2 is the no-slip condition $u_2 = 0$ or $u_2^D = -u^\infty$. In this derivation, the outer surface S_2 extends to infinity. In practice, we shall see that a finite radius of moderate size yields negligible errors in the computed solution.

With the foregoing discussion, one may write expressions (10) for each fluid phase and combine the results to achieve an integral formula

$$\Omega \, u(x_0) - \Omega_\infty \, u^\infty(x_0) = - \int_{S_2} \left[S \cdot (f_2 - f^\infty) - \mu T \cdot (u_2 - u^\infty) \cdot n \right] \, \mathrm{d}S$$

$$+ \int_{S_1} \left[S \cdot f_1 - \lambda \mu T \cdot u_1 \cdot n \right] \, \mathrm{d}S$$

$$- \int_{\Gamma} \left[S \cdot (\Delta f - f^\infty) - \mu T \cdot ((1 - \lambda)u - u^\infty) \cdot n \right] \, \mathrm{d}S \qquad (11)$$

which gives the velocity for a point located on the boundary surfaces. The coefficient Ω takes values $4\pi\mu(1 + \lambda)$, $4\pi\lambda\mu$ and $4\pi\mu$ for points x_0 on surfaces Γ, S_1 and S_2 respectively. The coefficient Ω_∞ takes the value $4\pi\mu$ for points x_0 on the surfaces Γ and S_2, and zero for points on the surface S_1. We have taken the unit normal to point into the volume of fluid 2 and out of the volume of fluid 1. This yields a consistent definition on the interface Γ.

For a boundary value problem with known velocity, the integral formula (10) combined with the boundary data yields an integral equation for the unknown surface stresses. For a droplet with interfacial boundary conditions (5), (6), the integral formula (11) yields an integral equation for the velocity at the interface and the unknown stresses or velocities on the outer boundaries. In the Newton iteration procedure described below, we shall make use of both of these results.

2.2. *Implementation of Newton iteration*

The boundary integral formulation above provides an efficient method for determining the velocity and stress on an interface of prescribed shape. We now develop an efficient procedure for determining equilibrium interfaces. Our basic approach is to adopt a boundary perturbation scheme analogous to that used in asymptotic analyses. In this procedure, we solve the boundary integral equations for a surface of known shape subject to the boundary conditions (5), (6) requiring continuity of velocity and stress at the interface. We then consider arbitrary perturbations of the boundary shape to determine the interface which satisfies the additional constraint imposed by the kinematic condition (7). It should be noted that the Newton method presented in this section is the three-dimensional analogue of the method presented by DH for two-dimensional problems.

Let an interface of known shape be designated Γ_0 and let the positions along this surface be identified as $\boldsymbol{x}_0(\xi, \eta)$ where ξ, η are the two parametric variables describing the surface. Let positions along a second interface Γ be defined by points $\boldsymbol{x}(\xi, \eta)$. Define the displacement $d(\xi, \eta)$ such that points on Γ are related to points on Γ_0 by

$$\boldsymbol{x}(\xi, \eta) = \boldsymbol{x}_0(\xi, \eta) + d(\xi, \eta)\, \boldsymbol{p}(\xi, \eta), \tag{12}$$

where $\boldsymbol{p}$ is a prescribed vector. (In effect, we will search for new surfaces Γ by specifying the *direction* of displacement $\boldsymbol{p}$, and solving for the *magnitude* of the displacement d.)

Using (12), the geometric variables describing the surface Γ can be expressed, with an error of $O(d^2)$, in terms of the corresponding variables on Γ_0 and known functions and derivatives of d. In this fashion, the unit normal vectors $\boldsymbol{n}$ and $\boldsymbol{n}_0$ on Γ and Γ_0 respectively are connected by

$$\boldsymbol{n} = \boldsymbol{n}_0 + \boldsymbol{n}'(d) + O(d^2). \tag{13}$$

The explicit form of the function $\boldsymbol{n}'(d)$ is given in the Appendix (equation (A 5)).

Let the interface Γ be considered as a perturbation of the interface Γ_0. The velocity on the interface Γ may then be written as a Taylor series about the unperturbed surface Γ_0 with a different expansion for each fluid. (This follows the classic perturbation procedure for a two-phase system.) Define a local Cartesian coordinate system $\boldsymbol{x}^L$ at the point $\boldsymbol{x}_0$ with the x_1^L- and x_2^L-axes in the tangent plane and the x_3^L-axis parallel to the normal vector $\boldsymbol{n}_0$. For the interior and exterior fluids, the velocity on Γ becomes

$$(\boldsymbol{u}_1)_\Gamma = (\boldsymbol{u}_1)_{\Gamma_0} + \sum_{i=1}^{3} \left(\frac{\partial \boldsymbol{u}_1}{\partial x_i^L} \right)_{\Gamma_0} p_i^L\, d + O(d^2), \tag{14}$$

$$(\boldsymbol{u}_2)_\Gamma = (\boldsymbol{u}_2)_{\Gamma_0} + \sum_{i=1}^{3} \left(\frac{\partial \boldsymbol{u}_2}{\partial x_i^L} \right)_{\Gamma_0} p_i^L\, d + O(d^2), \tag{15}$$

where p_i^L are the components of the vector $\boldsymbol{p}$ with respect to the local Cartesian system.

All velocities $\boldsymbol{u}$ in (14), (15) represent the solution for a boundary value problem (1)–(6) specified on surface Γ. Our goal in the perturbation analysis is to reformulate this as a modified boundary value problem on the known surface Γ_0. Toward this end, let $\bar{\boldsymbol{u}}, \bar{\boldsymbol{\sigma}}$ designate the solution of (1)–(6) for a droplet with unperturbed interface Γ_0 with both quantities evaluated on the interface. For small perturbations, we have

$$(\boldsymbol{u}_1)_{\Gamma_0} = \bar{\boldsymbol{u}} + O(d), \tag{16}$$

$$(\boldsymbol{u}_2)_{\Gamma_0} = \bar{\boldsymbol{u}} + O(d). \tag{17}$$

We subtract (14) from (15) and note that the left-hand side is zero from the continuity of $\boldsymbol{u}$ on Γ. We use (16) and (17) to evaluate the derivative and note that the tangent derivatives cancel owing to the continuity of $\bar{\boldsymbol{u}}$ on Γ_0. The result is

$$(\boldsymbol{u}_2 - \boldsymbol{u}_1)_{\Gamma_0} = -\left(\frac{\partial \bar{\boldsymbol{u}}_2}{\partial n} - \frac{\partial \bar{\boldsymbol{u}}_1}{\partial n}\right)_{\Gamma_0} (\boldsymbol{p} \cdot \boldsymbol{n}_0)\, d, \tag{18}$$

where $\partial/\partial n$ is equivalent to $\partial/\partial x_3^L$. In effect, we have transferred the velocity boundary condition (5) for the perturbed solution to the unperturbed boundary Γ_0.

Proceeding in a similar fashion, we may transfer the stress boundary condition (6) to the unperturbed surface. Here we must expand $\boldsymbol{\sigma}$ in a Taylor series, and then take the inner product with $\boldsymbol{n}$ on the perturbed surface Γ. After some algebra, the result is

$$(\boldsymbol{f}_2 - \boldsymbol{f}_1)_{\Gamma_0} = -\mathscr{F} d - (\bar{\boldsymbol{\sigma}}_2 - \bar{\boldsymbol{\sigma}}_1)_{\Gamma_0} \cdot \boldsymbol{n}' + \gamma(\nabla \cdot \boldsymbol{n})\boldsymbol{n} + (\rho_2 - \rho_1)(\boldsymbol{g} \cdot \boldsymbol{x})\boldsymbol{n}, \tag{19}$$

where

$$\mathscr{F} = \sum_{i=1}^{3} p_i^L \left(\frac{\partial \bar{\boldsymbol{\sigma}}_2}{\partial x_i^L} - \frac{\partial \bar{\boldsymbol{\sigma}}_1}{\partial x_i^L}\right)_{\Gamma_0} \cdot \boldsymbol{n}_0. \tag{20}$$

The curvature term $\gamma(\nabla \cdot \boldsymbol{n})\boldsymbol{n}$ in (19) may be expressed in terms of its unperturbed value and functions and derivatives of d, as described in the Appendix. The gravitational term $(\rho_2 - \rho_1)(\boldsymbol{g} \cdot \boldsymbol{x})\boldsymbol{n}$ may by expressed easily in terms of its unperturbed value and functions of d by applying (12) and (13).

With (18) and (19), we now have boundary conditions for the velocity and stress for the perturbed boundary value problem expressed as conditions on the unperturbed interface Γ_0. Thus we may choose an arbitrary d and solve for any surface Γ by using the same boundary integral equation on Γ_0 changing only the boundary data in (18) and (19). Specifically, with these boundary conditions, the boundary integral formula (11) generalizes to

$$\begin{aligned}
\Omega_1\, \boldsymbol{u}_1(\boldsymbol{x}_0) &+ \Omega_2\, \boldsymbol{u}_2(\boldsymbol{x}_0) - \Omega_\infty\, \boldsymbol{u}^\infty(\boldsymbol{x}_0) \\
&= -\int_{S_2} \left[\boldsymbol{S} \cdot (\boldsymbol{f}_2 - \boldsymbol{f}^\infty) - \mu\boldsymbol{T} \cdot (\boldsymbol{u}_2 - \boldsymbol{u}^\infty) \cdot \boldsymbol{n}\right]\, \mathrm{d}S \\
&\quad + \int_{S_1} \left[\boldsymbol{S} \cdot \boldsymbol{f}_1 - \lambda\mu\boldsymbol{T} \cdot \boldsymbol{u}_1 \cdot \boldsymbol{n}\right]\, \mathrm{d}S \\
&\quad - \int_{\Gamma_0} \left[\boldsymbol{S} \cdot (\boldsymbol{f}_2 - \boldsymbol{f}_1 - \boldsymbol{f}^\infty) - \mu\boldsymbol{T} \cdot (\boldsymbol{u}_2 - \lambda\boldsymbol{u}_1 - \boldsymbol{u}^\infty) \cdot \boldsymbol{n}\right]\, \mathrm{d}S,
\end{aligned} \tag{21}$$

where the coefficient Ω_1 is $4\pi\lambda\mu$ for points $\boldsymbol{x}_0$ on Γ_0 and S_1, and zero for points on S_2; while Ω_2 is $4\pi\mu$ for points $\boldsymbol{x}_0$ on Γ_0 and S_2, and zero for points on S_1.

The boundary integral equation (21) presents an efficient approach for studying a large number of trial surfaces Γ. The discretized form of this equation yields a linear system of algebraic equations $\boldsymbol{A}\boldsymbol{x} = \boldsymbol{b}$ for the unknown surface velocities. The system matrix for these equations is a function only of the unperturbed shape Γ_0, while the perturbation d defining Γ affects only the right-hand side. Thus the solution for each successive Γ requires no additional numerical quadratures, and negligible computational effort if the equations are solved by Gaussian elimination, and the LU factorization is stored from a previous solution. While this is indeed an efficient approach, we may go one step further. If we leave d unspecified and enforce the kinematic condition (7) on the perturbed surface Γ, we obtain an additional equation

which may be used to solve for d. Using (14), we transfer the kinematic condition on Γ to the unperturbed surface Γ_0, and find

$$(\boldsymbol{u})_{\Gamma_0} \cdot \boldsymbol{n}_0 = -\bar{\boldsymbol{u}} \cdot \boldsymbol{n}' - \sum_{i=1}^{3} p_i^L \left(\frac{\partial \bar{\boldsymbol{u}}}{\partial x_i^L} \right)_{\Gamma_0} \cdot \boldsymbol{n}_0 \, d. \qquad (22)$$

The kinematic condition (22) applies to both $\boldsymbol{u}_1$ and $\boldsymbol{u}_2$; however, specifying either guarantees the other owing to the continuity of velocity (5). The kinematic condition may be used to eliminate one component of the unknown velocity vector at the interface. The unknown displacement d takes its place, leaving the same number of unknowns as in the previous integral equations.

The steps in the Newton iteration for the equilibrium interface Γ are as follows:

Step 1: solve (11) with boundary conditions (5) and (6) to find the velocity $\bar{\boldsymbol{u}}$ on the interface Γ_0.

Step 2: with the velocity $\bar{\boldsymbol{u}}$ known, solve an equation of the form (10) for the surface stresses $\bar{\boldsymbol{f}}_1, \bar{\boldsymbol{f}}_2$. (The boundary condition (6) gave only the jump $\Delta \boldsymbol{f}$, and not the individual stresses.) This requires a single boundary integral equation solution, because the stresses are related by $\bar{\boldsymbol{f}}_2 = \bar{\boldsymbol{f}}_1 + \Delta \boldsymbol{f}$ with $\Delta \boldsymbol{f}$ known.†

Step 3: evaluate the derivatives $\partial \bar{\boldsymbol{u}}/\partial \boldsymbol{x}^L$, $\partial \bar{\boldsymbol{\sigma}}/\partial \boldsymbol{x}^L \cdot \boldsymbol{n}_0$ required for boundary data in (18), (19) and (22).

Step 4: solve (21) with boundary conditions (18), (19) and (22) and with constant drop volume, to determine the displacement d as described above.

This procedure requires three boundary integral solutions per iteration; however the kernels $\boldsymbol{S}$ and $\boldsymbol{T}$ are identical in each case and numerical quadratures need be executed only once. The tangent derivatives $\partial/\partial x_i^L$, $i = 1, 2$, in Step 3 are evaluated by differentiation of known quantities along the surface. The normal derivatives $\partial/\partial n$ required for (18), (19) and (22) may be evaluated indirectly given the known values $\bar{\boldsymbol{u}}$ and $\bar{\boldsymbol{\sigma}}$ and their derivatives along the surface as well as the equations $\nabla \cdot \bar{\boldsymbol{u}} = 0$, $\nabla \cdot \bar{\boldsymbol{\sigma}} = 0$. All numerical derivatives are evaluated using the so-called collocation derivative, that is using analytical differentiation of the high-order polynomials which comprise the basis functions for the spectral element expansions. See Muldowney & Higdon (1995) or Canuto *et al.* (1988, §§ 2.3, 2.4) for additional details.

A comment may be warranted concerning the constant-volume constraint in Step 4. While the solution of the boundary integral equation yields a velocity field which is divergence free, the boundary perturbation represented by d admits a broad class of surfaces which may include different volumes of fluid. We add the volume constraint to assure that the equilibrium interface corresponds to the specified fluid volume V_0.

In the Newton iteration procedure, we assume that the direction of the search vector $\boldsymbol{p}$ is specified *a priori*. For freely suspended droplets, a reasonable choice is simply the unit normal vector $\boldsymbol{n}$. For droplets attached to a plane wall, we need to modify this choice, because a displacement in the normal direction would move the end points of the interface away from the wall. We need to define $\boldsymbol{p}$ such that the end points are free to move along the wall, but remain in the plane $z = 0$. As an obvious choice, we define $\boldsymbol{p}(\xi, \eta)$ parallel to the wall at the end points and smoothly interpolate to $\boldsymbol{n}$ as $\boldsymbol{x}(\xi, \eta)$ moves away from the wall. This choice admits a class of interfaces Γ with arbitrary contact angles and arbitrary contact positions along the wall.

---

† As an alternative to Step 2, the surface stress may be evaluated directly as an integral of $\Delta \boldsymbol{f}$ and $\boldsymbol{u}$ over the boundary surfaces. The kernels required for this integration are given in Muldowney & Higdon (1995). These kernels require additional time for numerical quadratures, and the preferred choice will be dictated by a balance between quadrature effort and matrix inversion time.

2.3. *Implementation of optimization iteration*

As has already been stated, we seek the optimal shape of the contact line which determines the minimum hysteresis $\theta_A - \theta_R$ for given capillary number Ca, advancing contact angle θ_A and position of the leading point x_1. The optimization problem may be stated as:

$$\text{for all contact lines } C, \text{ minimize: } \theta_A - \theta_R \tag{23}$$

subject to:

$$\theta_i \leqslant \theta_A, \tag{24}$$

$$\theta_i \geqslant \theta_R, \tag{25}$$

$$x_1 \equiv \text{fixed} \qquad \text{or} \qquad d_1 = 0, \tag{26}$$

and to the system of equations (1)–(7),

where θ_i, $i = 1, \ldots, N_{cl}$, are the contact angles along the contact line C, N_{cl} the number of contact line points and θ_R the desired maximum receding contact angle.

Before proceeding with this problem, we note one important point concerning the number of independent variables describing the contact line. While there are N_{cl} collocation points along the contact line, resulting from the interface discretization, we have fewer degrees of freedom owing to constraints on the smoothness of the contact line. On smooth boundary surfaces, we require that the contact lines have continuous slope and curvature. This reduces the degrees of freedom by 2 on each spectral element. These constraints would not be enforced if geometrical shapes involving sharp edges introduced discontinuities in the contact line.

The nonlinear optimization problem presented by equations (23)–(26) is regularly encountered in the optimization literature. These problems are most often addressed by algorithms in the general class of sequential quadratic programming methods, SQP (Biegler *et al.* 1997). In these algorithms, the nonlinear objective function (23) is replaced by a local quadratic approximation and efficient techniques are used to solve the quadratic programming problem to yield a new prediction for the optimal solution. An updated quadratic approximation is constructed based on the new estimate, and the process is repeated until convergence. In the present circumstances, we find it inconvenient to employ the SQP approach, because the boundary integral formulation does not provide easy access to the higher-order parametric derivatives needed to form the quadratic approximations. In its place, we rely on a simpler approach based on successive linear programming. A linear approximation to the objective function is constructed, and a linear optimization problem is solved to find the new prediction for the solution. An updated linearization is performed, and the process is repeated until convergence. The successive linear optimization procedure is the analogue of Newton's method for constrained optimization problems. Its radius of convergence is smaller than that of SQP methods; however this limitation is easily overcome by parameter continuation from nearby solutions.

To implement this optimization procedure, we must determine the relation between the contact angles θ and the position of the contact points (or their displacement d^{cl}). The contact angles of the unknown contact line C may be written formally as a Taylor series about the known contact line C_0 of an equilibrium interface Γ

$$(\theta_i)_C = (\theta_i)_{C_0} + \sum_{j=1}^{M_{cl}} \left(\frac{\partial \theta_i}{\partial d_j^{cl}} \right)_{C_0} d_j^{cl} + O(d^2), \quad i = 1, \ldots, N_{cl}, \tag{27}$$

where M_{cl} is the number of independent variables describing the contact line. The unknown derivative matrix $(\partial\boldsymbol{\theta}/\partial\boldsymbol{d}^{cl})_{C_0}$ is computed numerically by finite differences based on solutions for distinct values of the displacements d_j^{cl}. As a first step, we compute the equilibrium surface Γ for a given contact line C_0 and $d_j^{cl} \equiv 0$. At the next step, a point on the contact line is perturbed with a small displacement, and the new equilibrium shape and associated contact angles are computed. This process is repeated until all columns of $(\partial\boldsymbol{\theta}/\partial\boldsymbol{d}^{cl})_{C_0}$ have been calculated. For each step in this process, the system matrix is the same as the original matrix and only the right-hand-side data are changed. Thus minimal computational effort is involved.

With the linearization introduced by (27), the system of equations (23)–(27) constitutes a linear programming problem which we solve using the Simplex method. The linear optimization problem may be solved for either the contact angles or the displacements. We choose to solve for the displacements and recover the contact angles using (27).

Given the procedure outlined above, the full solution for the optimal contact line and the associated equilibrium interface shape requires successive application of Newton iterations and linear programming steps. In a typical problem, 2 to 3 optimization iterations are sufficient to reduce the displacement d^{cl} at the contact line below 10^{-4}. Each optimization iteration requires four Newton iterations to compute the equilibrium surface Γ for a given contact line C_0, and one Newton iteration to calculate the derivative matrix $(\partial\boldsymbol{\theta}/\partial\boldsymbol{d}^{cl})_{C_0}$.

In §3 below, we shall present a wide range of solutions for the optimal contact line contours and interface shapes. While these contours represent the true solutions of the optimization problem described above, a question arises as to whether a droplet starting in a quiescent fluid would arrive at the true optimal shape as the flow rate or Ca is increased. In certain circumstances, the evolution of the contact line might help to determine the final contour of the contact line.

To investigate these issues, we will consider alternative optimization problems based on the system (23)–(27) with additional constraints. We seek the optimal contact line shape under the restriction that the $|y|$-position of the contact points should not exceed the maximum initial y-position $|y_0^{max}|$. This requirement introduces the following constraints to the linear programming problem:

$$-|y_0^{max}| \leqslant y_i \leqslant |y_0^{max}|, \quad i = 1,\ldots,N_{cl}. \tag{28}$$

Finally, to compare our optimal results with the commonly used circular contact lines, we also seek the optimal shape based on circular contours of arbitrary radius. Starting from an initial circular shape, the constraint (26) is removed and replaced by

$$d_i \equiv \text{constant} = d_{i+1}, \quad i = 1,\ldots,N_{cl}-1. \tag{29}$$

2.4. *Numerical methods*

The numerical solution of the boundary integral equation of §2.2 is achieved through the spectral boundary element method (Occhialini *et al.* 1992; Muldowney & Higdon 1995). Briefly, each boundary is divided into a small number of surface elements which are parameterized by two variables ξ and η on the square interval $[-1,1]^2$. The geometry and physical variables are discretized using Lagrangian interpolation in terms of these parametric variables. The base points (ξ_i,η_i) for the interpolation are chosen as the zeros of orthogonal polynomials of Gauss-type. This is equivalent to an orthogonal polynomial expansion and yields the spectral convergence associated with such expansions. The discretizations are substituted into the appropriate boundary

integrals and quadratures evaluated using adaptive Gaussian quadrature. Further details are given in the aforementioned references.

The general boundary integral equation (10) admits two different types of points. The collocation points of the left-hand side where the equation is required to hold and the basis points of the right-hand side where the physical variables u and f are defined. The spectral element method as implemented here employs collocation points of Legendre–Gauss quadrature, i.e. in the interior of the element. As a result the boundary integral equation holds even for singular elements, i.e. the elements which contain the contact line where the normal vector is not uniquely defined.

In addition, we use basis points of Legendre–Gauss–Lobatto quadrature (Canuto *et al.* 1988, §2.2.3, 2.3). Owing to this choice, the position is always continuous on the interface. Note that the points $x(\xi, \eta)$ on the surface Γ are connected through the variables $d(\xi, \eta)$ with the basis points. Additional constraints are required at the ends of the elements to enforce continuity of the normal vector and curvature on the interface, i.e. the term $(\nabla \cdot n)n$. The boundary conditions on the contact angle and/or contact line position must be added as further constraints for the linear system. The discretized system of equations is then solved using a least-squares algorithm from the LAPACK software library.

The problem studied in this paper admits one level of symmetry about the plane $x = 0$. Exploiting this symmetry reduces the memory requirements by a factor of 2^2, the computational time for the system matrices by a factor of 2 and the solution time for the linear systems by factor of 2^3. All the computations were performed on IBM RISC6000/3CT workstations and on multiprocessor computers including SGI Cray Origin 2000 and HP-Convex Exemplar SPP 2000. Multiprocessor runs exploit the parallel nature of calculating the system matrices resulting in a nearly linear decrease in c.p.u. time.

3. Results

In this section, we present the results of a comprehensive series of computations based on the methods described in §2. Numerous tests were conducted to verify the reliability and robustness of these algorithms. The performance of the basic spectral element algorithm has been documented previously (Occhialini *et al.* 1992; Muldowney & Higdon 1995). The two-dimensional implementation of the present method was tested as described by DH. For the present implementation of the Newton method, various discretizations were employed with the number of polynomial basis points N_B ranging from 4 to 12; exponential convergence was demonstrated, comparable to that in previous applications of this algorithm. Several additional tests were performed to verify the performance of the Newton iteration procedure. Two classes of tests were conducted: for freely suspended droplets and for droplets attached to a plane wall.

For the freely suspended droplets, equilibrium shapes were compared with the asymptotic theory by Barthès-Biesel & Acrivos (1973) (their figures 2 and 3) and with computational results by Higdon & Schnepper (1994) (their tables 5.4.2 and 5.4.3). For the attached droplets, detailed comparisons were made with the results of Li & Pozrikidis (1996) (their figure 6) for the case of a fixed contact line of circular shape and $\lambda = 1$. Additional comparisons were made with the results by Milinazzo & Shinbrot (1988) (their figure 20) and Brown, Orr & Scriven (1980) (their figure 5) for the case of the gravitational deformation of drops on inclined planes when the contact line remains a fixed circle. All computations were in excellent agreement with earlier results.
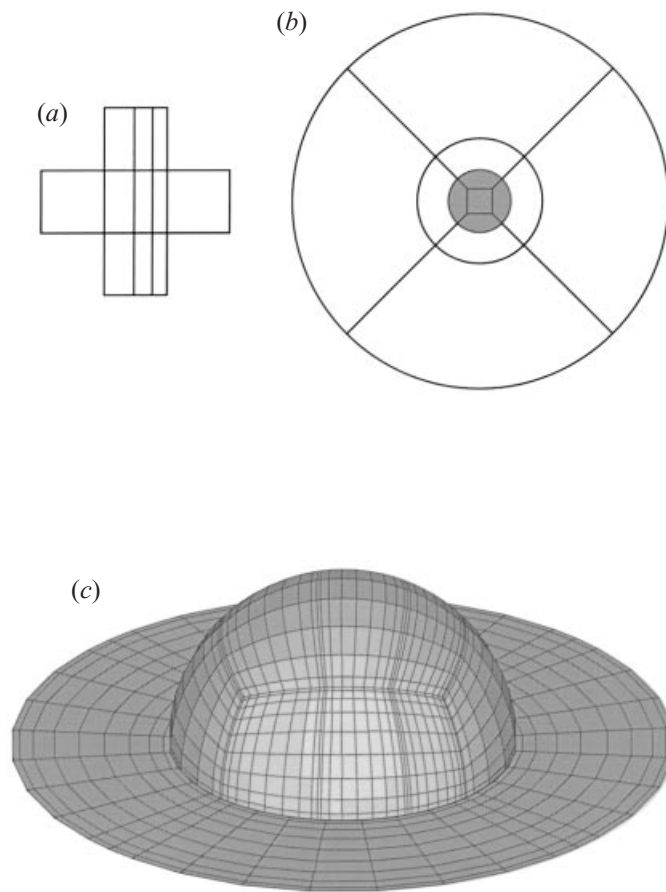
FIGURE 3. Discretization of geometry for spectral boundary element calculations. (*a*) Layout of element panels for the drop surface Γ. (*b*) Layout of element panels for the solid surfaces S_1 (shaded area) and S_2. (*c*) Three-dimensional view illustrates Lobatto distribution of nodal lines for the total geometry.

In the present paper, the majority of computations were performed with a discretization employing 24 elements. The surface of the drop is projected onto a cube whose faces are subdivided into a total of 11 elements, as shown in figure 3 (*a*). As will be shown later, the optimal shape of the contact line involves an acute jump in the distribution of the contact angles (see figure 4 *c* below). Therefore the spectral points must be concentrated on the drop surface close to where the jump occurs. Failure to do this will result in poor accuracy in determining the minimum hysteresis $\theta_A - \theta_R$. While several discretizations of the drop surface were considered, we found that the aforementioned strategy provided the most efficient solution.

The inner solid surface S_1 is discretized into five elements and the outer solid surface S_2 into two rows of four elements each, as shown in figure 3 (*b*). The distribution of elements on these two surfaces is based on the discretization of the contact line. The discretization of the entire geometry is shown in figure 3 (*c*). As discussed in §2.1, the outer surface S_2 is required to extend to infinity. In practice, a finite radius for the surface S_2 may be chosen with negligible change in the predicted yield conditions. Extensive tests were performed to determine the errors for this approximation with

N_B	Fixed circle $Ca = 0.08$	Unconstrained $Ca = 0.01$	Unconstrained $Ca = 0.08$
4	−17.1720		
5	0.7714	−0.2398	0.5912
6	−0.5129	−0.0084	−0.4207
7	−0.2396	−0.0042	−0.2538
8	0.0097	0.0009	−0.1187
9	46.6509	4.3501	32.8990

TABLE 1. Error in the computed contact angle hysteresis $\theta_A - \theta_R$. N_B is the number of Lagrangian interpolation points in the spectral element discretization. Columns 2 to 4 report the error in hysteresis $\theta_A - \theta_R$ with respect to the value of $\theta_A - \theta_R$ for the maximum value of N_B, which is reported in the last entry of each column. Column 2 is for a fixed contact line of circular shape, with $\lambda = 1$ and initial angle of $\theta = 90°$. The last two columns are for an unconstrained contact line, with $\lambda = 1$ and $\theta_A = 90°$ and for two different capillary numbers Ca. All results were computed with a discretization employing 24 elements.

the radius of S_2 ranging from 2 to 40 times the radius of wetted area S_1. A ratio of S_2/S_1 radii equal to 3 was sufficient to produce a change in $\theta_A - \theta_R$ of less than 1 %, while a ratio of 10 lead to a relative change of less than 5×10^{-4}. Given these results, a ratio of 10 was chosen for the computations in this paper.

For the majority of the results presented in this section, a spectral expansion with $N_B = 7$ points was used on each element. For certain cases with $\theta_A = 50°$, additional points were used up to $N_B = 9$. For $\theta_A = 30°$, the hysteresis $\theta_A - \theta_R$ and the jump are small; however, many points are required throughout the drop surface. In this case, the drop surface was divided into five elements with $N_B = 10$. Convergence for the spectral element computations and for the optimization procedure was verified by increasing the number of spectral points N_B and determining the change in the computed hysteresis $\theta_A - \theta_R$. A selection of test results is presented in table 1. In all cases, the results show a rapid decrease in the discretization error with increasing number of basis points. The results for the fixed circle test only the Newton algorithm, while the unconstrained cases also test the optimization algorithm. For small deformation (unconstrained droplet, $Ca = 0.01$), a relative error of 2×10^{-4} is achieved with $N_B = 8$ basis points. For the larger deformations (circle and unconstrained drop at $Ca = 0.08$), a relative error $\leqslant 4 \times 10^{-3}$ is achieved.

The Newton method implemented in this paper has proven to be a robust procedure, of high accuracy and efficiency, with a wide range of convergence. When the Newton iteration is combined with the successive linear programming algorithm, we find that the range of convergence is somewhat reduced, especially for problems with sharp changes in the contact angles around the contact line contour. Owing to these issues, the range of deformations computed in this paper (as represented by the range of contact angle hysteresis $\theta_A - \theta_R$) is not as large as that presented in our paper on the two-dimensional displacement problem.

In the following sections, we present the optimal shape of the contact line which determines the maximum flow rate (or Ca) for which a droplet can adhere to the surface in Stokes shear flows. The relevant parameters in this problem are the capillary number Ca, the viscosity ratio λ, the advancing contact angle θ_A, the receding contact angle θ_R or equivalently the hysteresis $\theta_A - \theta_R$, the Bond number B_d and in the general case of an inclined plane, the inclination angle β. We exclude gravitational effects in

the present paper (setting $B_d = 0$), but address these effects in a companion paper (Dimitrakopoulos & Higdon 1998). We conduct a detailed study of the effects of the remaining parameters, presenting results for the critical Ca as a function of $\theta_A - \theta_R$ for several fixed values of the advancing contact angle θ_A (mainly $\theta_A = 30°, 50°, 70°, 90°$) and of the viscosity ratio λ (mainly $\lambda = 0, 1, 10$).

3.1. *Influence of the advancing contact angle θ_A for a viscous drop with $\lambda = 1$*

We begin our investigation of drop displacement from a rigid wall by considering the influence of the advancing contact angle θ_A on the critical capillary number Ca for a viscous droplet with $\lambda = 1$. Figure 4 (*a,b*) shows the contact line contours and the drop profiles (drop surface intersection with the plane $y = 0$) for a drop with viscosity ratio $\lambda = 1$, advancing contact angle $\theta_A = 90°$ and for several values of the capillary number Ca.

With each successive curve, a larger Ca is specified, and a larger contact angle hysteresis is required to hold the drop in place. The distribution of contact angles around the drop contours is shown in figure 4 (*c*), while figure 4 (*d,e*) shows three-dimensional views for a typical droplet shape. Two noteworthy features are apparent from these figures. First (see figure 4 *a*), we observe that the downstream edge of the contact line is displaced further as the flow rate is increased. This is similar to the behaviour of two-dimensional droplets. As the hydrodynamic forces on the droplet increase, the net interfacial force must be increased by reducing the contact angle on the front of the droplet. With a smaller angle, the droplet spreads over a larger area to accommodate the same fluid volume. The second noteworthy feature is that the width of the contact line in the *y*-direction increases as the flow rate is increased. This feature is of interest for a number of reasons. On first impression, it would seem more likely that a droplet should spread in the flow direction, and not in the transverse direction; however, a simple physical argument reveals the logic of this transition. If a droplet spreads in the flow direction, the long sides of the drop yield interfacial forces at the contact line which pull sideways and do not act to counter the flow. By contrast, if the droplet spreads in the transverse direction, the increased width of the contact line on the front and back increases the net interfacial force which is proportional to $\theta_A - \theta_R$ multiplied by the width. The increased width and the reduced contact angle both act to increase the interfacial force. Thus the most stable drop for a given volume has the wide asymmetrical profile illustrated in figure 4 (*a*). While the contours seen in these figures represent the optimal (most stable) contact lines a droplet may achieve, they are not necessarily the contours which will be seen in an experiment when a droplet is placed in a quiescent fluid and the fluid velocity is monotonically increased. We shall return to this issue in the discussion below.

While we have focused on the shape of the contact line, the variation of the contact angle around the contour also has an important effect on the force balance. Figure 4 (*c*) shows the variation of the contact angle θ along the contact line as a function of the azimuthal angle ϕ for the stated values of λ, θ_A and Ca. The azimuthal angle ϕ is measured with respect to the positive *x*-direction as usual. This figure shows that the downstream portion of the contact line admits a single maximum contact angle (the advancing angle θ_A) while its upstream portion admits a single minimum angle (the receding angle θ_R). Between these two portions there is an acute jump in the distribution of the contact angles which occurs for $\phi \approx 55°–90°$ and $\phi \approx 270°–305°$. These locations are noted as dashed lines on the contact line contours in figure 4 (*a*). The sharp jump in contact angle is a further consequence of the droplet attempts to maximize the interfacial force. The drop holds the minimum
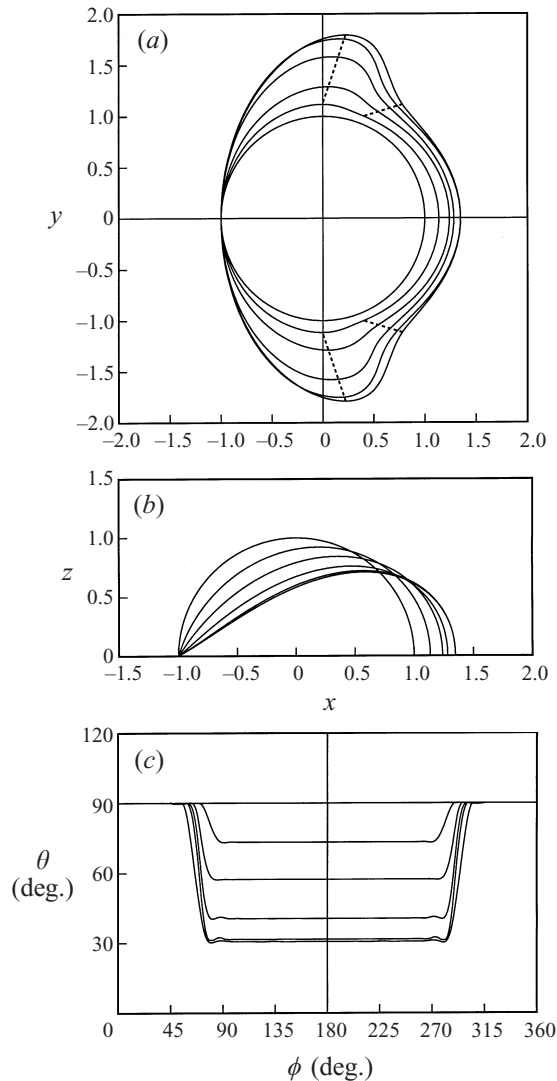
FIGURE 4 (*a–c*). For caption see facing page.

contact angle over the entire front of the contact line, then makes the fastest possible transition to the maximum angle on the rear-facing contour. The sharp jump in contact angle observed here is in distinct contrast to the smooth distribution observed in simulations for circular contact lines (Li & Pozrikidis 1996). Finally, with respect to the numerical computations, we note that this jump presents a significant challenge to the numerical algorithm, and it is important to concentrate grid points near the jump to accurately capture the sharp change in the interfacial shape.

Having explored the basic principles associated with the deformation and displacement of the droplet, we turn our attention to the prediction of the yield conditions as a function of the drop parameters. Figure 5 shows the critical *Ca* as a function of the contact angle hysteresis $\theta_A - \theta_R$ for several values of θ_A and for the viscosity ratio $\lambda = 1$. For each point on a given curve, we specify the capillary number and a fixed value of θ_A, and then find the optimal solution which minimizes the hysteresis

(*d*)

(*e*)
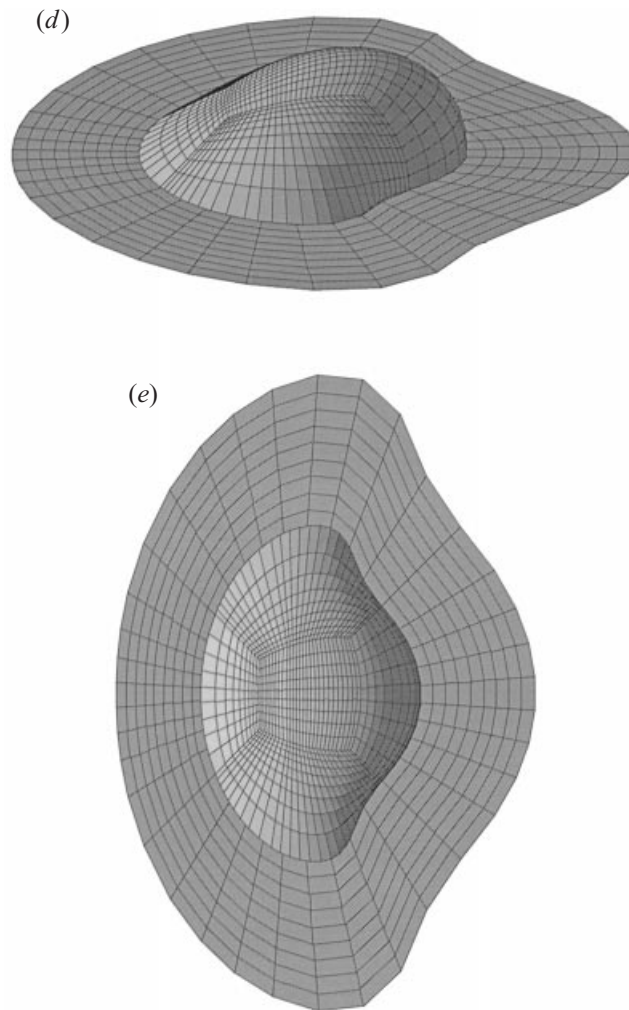
FIGURE 4. Equilibrium shapes for droplets in shear flows with viscosity ratio $\lambda = 1$ and advancing contact angle $\theta_A = 90°$. For (*a–c*) the capillary number is $Ca = 0$, 0.04, 0.08, 0.12, 0.14, 0.1425. (*a*) The optimal shape of the contact line. The dashed lines show the location of the jump region. (*b*) The cross-section of the drop surface with the plane $y = 0$. (*c*) The variation of the contact angle θ as a function of the azimuthal angle ϕ. (*d,e*) The drop surface for capillary number $Ca = 0.1425$.

$\theta_A - \theta_R$. The specified Ca then represents the yield condition for that value of θ_A and $\theta_A - \theta_R$. The terminal points at the end of each curve represent the largest $\theta_A - \theta_R$ for which accurate numerical calculations could be executed. The criteria for an accurate numerical solution include convergence of the linear programming iteration and of the Newton iteration, consistency with increasing order of N_B and an error tolerance for the maximum $\boldsymbol{u} \cdot \boldsymbol{n} \neq 0$ on the interface. Our results show that for all the cases, the algorithm stops when the linear programming fails to converge. On physical grounds, it appears that the true terminal point corresponds to a value $\theta_A - \theta_R \to \theta_A$, for which $\theta_R \to 0$ and the interface becomes tangent to the boundary wall at the upstream portion of the contact line. We emphasize that figure 5 gives accurate yield conditions for the plotted parameter values. The only limitation is that we are unable to provide precise predictions for extreme values of the hysteresis $\theta_A - \theta_R$.
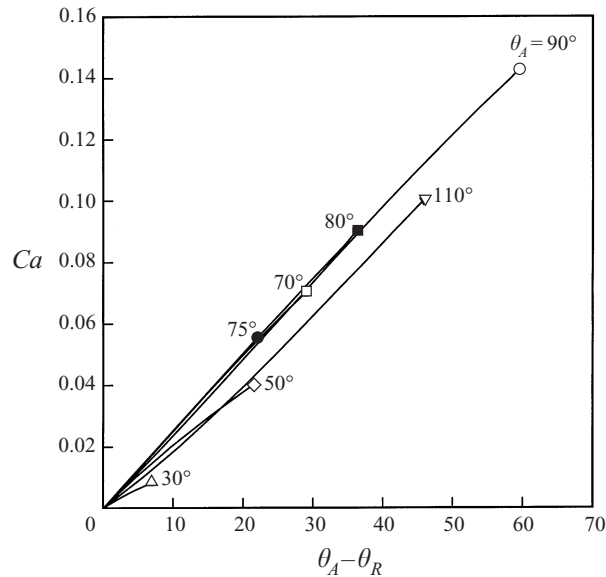
FIGURE 5. Critical capillary number Ca versus hysteresis $\theta_A - \theta_R$ for viscosity ratio $\lambda = 1$ and for the unconstrained optimization problem.

The curves of figure 5 reveal interesting behaviour for the critical Ca at different advancing contact angles θ_A for a viscous drop. For a given hysteresis $\theta_A - \theta_R$, increasing the contact angle θ_A from small values, *increases* the critical shear rate or Ca, for values of the advancing contact angle up to $\theta_A = 75°$–$80°$. (Note that the curves for $\theta_A = 75°$ and $\theta_A = 80°$ are nearly coincident.) Above these values, increasing the contact angle θ_A *decreases* the critical shear rate. Figure 5 shows that the critical capillary number Ca has a similar value for $\theta_A = 70°$–$90°$, but admits a much smaller value for $\theta_A = 110°$. Thus for three-dimensional droplets, we see that there is a local maximum in the required yield stress with the most stable droplets having a contact angle of approximately $\theta_A \approx 75°$. This behaviour is in contrast to the results for a two-dimensional droplet where a monotonic increase with θ_A was found.

At this time, we return to the subject of the contact line contours and consider how the conditions of an experiment might affect the observed shapes. Recall that the solutions presented in figure 4(a) represent optimal solutions independent of the initial configuration of a droplet. Consider a droplet with hysteresis $\theta_A - \theta_R$. Under quiescent conditions, this droplet may exist in an infinite number of configurations. If the droplet is formed by injecting liquid through a small hole in the substrate, it might form a section of a sphere with all contact angles having the value θ_A. Upon the initiation of flow, the rear of the contact line would immediately begin to move downstream as the value of θ_A is exceeded. This would lead to elongated droplets with shapes quite different from those shown in figure 4. The yield condition for these droplets may be less than for those with the optimal contours of figure 4. In another experiment, suppose one starts with the quiescent droplet as before, but extracts fluid until the drop just begins to recede, yielding a section of sphere with all contact angles equal to θ_R. When the flow is initiated for this droplet, it is the front of the droplet which will move first as the contact angle falls below θ_R. In this case, short wide droplets will form whose shape might well approach the optimal shapes shown

above. The important conclusion here is that the actual yield stress is determined not only by the maximum possible yield stress, but also by the initial configuration of the droplet, the conditions of the experiment and the evolution of the contact line.

To test the sensitivity of the yield stress subject to these conditions, we consider an alternative optimization problem. We seek to model the case of the quiescent droplet with contact angle θ_A whose initial distortion will lead to elongation in the flow direction. To address this problem, we allow the contact line to assume any shape consistent with the constraint $\theta_R \leqslant \theta \leqslant \theta_A$, but impose the further constraint that the magnitude of the lateral positions $|y|$ cannot exceed the maximum value $|y_0^{max}|$ in the initial configuration of a droplet with constant angle θ_A. This constraint forces the contact line to extend in the flow direction to accommodate the hydrodynamic forces imposed by the flow. We refer to solutions of this optimization problem as the *y-constrained* solutions.

Figure 6 (*a,b*) shows the contact line contours and the drop profiles for the *y*-constrained optimization for a droplet with viscosity ratio $\lambda = 1$, advancing contact angle $\theta_A = 90°$ and for several values of the capillary number *Ca*. As with the unconstrained optimization above, on each successive curve, a larger *Ca* is specified and a larger contact angle hysteresis is required to hold the drop in place. Figure 6 (*a*) shows that the downstream portion of the contact line has been displaced much further compared with that of the unconstrained optimal problem for the same values of the capillary number. This behaviour is to be expected because of the *y*-constraint in the shape of the contact line.

Figure 6 (*c*) shows the variation of the contact angle θ along the *y*-constrained contact line as a function of the azimuthal angle ϕ for the prescribed values of λ, θ_A and *Ca*. As before, the downstream portion of the contact line admits a single maximum contact angle θ_A, its upstream portion admits a single minimum contact angle θ_R, and there is an acute jump in the distribution of the contact angles which occurs for $\phi \approx 65°–120°$ and $\phi \approx 240°–295°$. The positions of the contact line at which the jump occurs are noted in figure 6 (*a*). It is of interest to note that for all values of *Ca*, the jump region begins at $\phi \approx 120°$ and $\phi \approx 240°$, while its size increases as the capillary number *Ca* is increased. The broader width of the jump region may be attributed to the more elongated shape of the contact line; that is, for drops with long sides parallel to the flow direction, the net interfacial force is insensitive to the position and width of the jump, because the interfacial force acts in a lateral direction on these sections. Comparing the figures 4 (*c*) and 6 (*c*), it is obvious that for the same value of the capillary number, the *y*-constrained contact line admits a smaller receding contact angle θ_R. This implies that the droplet requires more hysteresis to hold its position, i.e. that it is slightly less stable than the optimal solution. Figure 6 (*d,e*) shows two three-dimensional views of the drop for *Ca* = 0.09 for this problem. Comparison with the three-dimensional views in figure 4 shows the obvious differences between the drop shapes for the two optimization problems. It is of interest to note that the *y*-constrained contact line cannot be approximated with an ellipse, because for this shape, the contact angles change continuously along the contact line. In addition, the minimum angle θ_R for an ellipse is located not on the upstream portion of the contact line but somewhere between the upstream and the downstream portions (see Li & Pozrikidis 1996, figure 12*f*).

The yield conditions for droplets with the *y*-constrained contact lines are shown in figure 7 with the critical *Ca* plotted as a function of hysteresis $\theta_A - \theta_R$ for several values of θ_A and for the viscosity ratio $\lambda = 1$. The curves of this figure show that the influence of the advancing contact angle θ_A on the *y*-constrained viscous droplet is
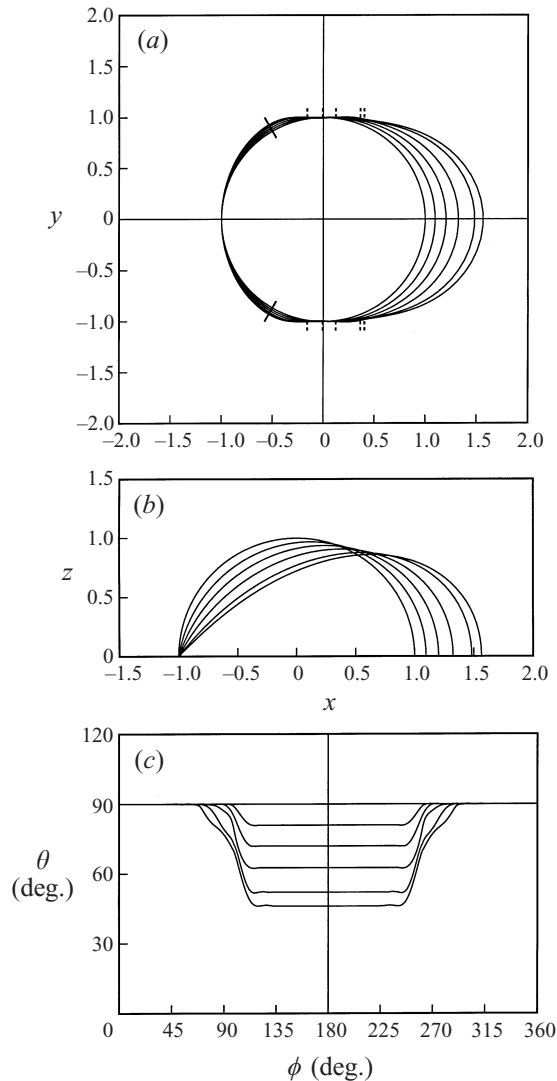
FIGURE 6 (*a*–*c*). For caption see facing page.

qualitatively similar to the unconstrained case. To compare these results more directly, we plot the two sets of curves in a single graph, in figure 8 (*a*) for $\theta_A = 90°$ and in figure 8 (*b*) for $\theta_A = 50°$. In each of these figures, we plot one additional curve, corresponding to the case of a circular contact line with the same maximum contact angle θ_A. This last curve is determined as the solution of the third optimization problem, mentioned in §2.3. The insets in each figure show the actual shape of the contact line contours for the three different optimization problems. The results plotted in figure 8 show that for large advancing contact angles θ_A, the critical capillary number *Ca* for the unconstrained optimization problem is higher than for the two other problems as expected. As the contact angle θ_A decreases, the difference in *Ca* for the unconstrained and the *y*-constrained problem becomes smaller and smaller, and for $\theta_A \leqslant 50°$ there is no practical difference. For all angles θ_A studied, we found that the circular contact line admits a significantly smaller capillary number. For a droplet

(d)

(e)
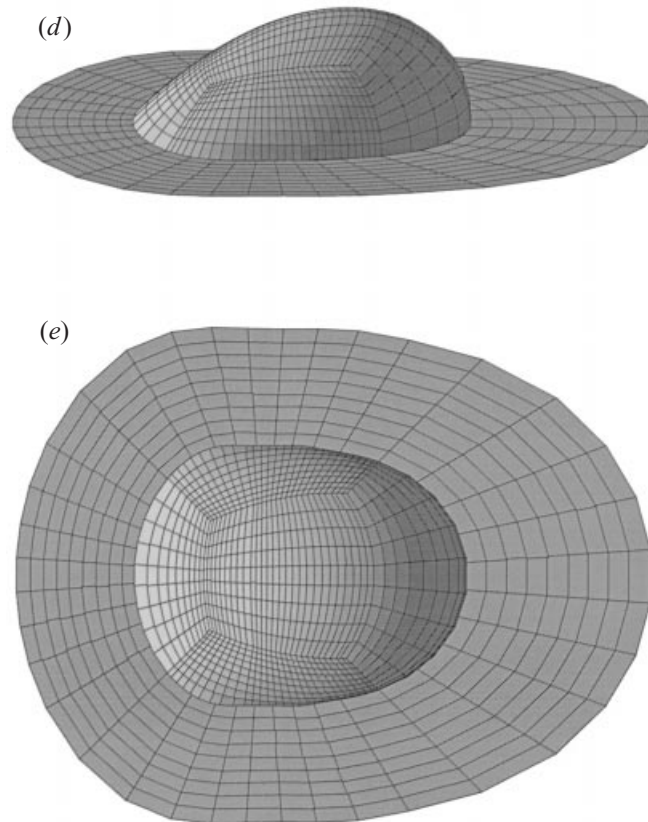
FIGURE 6. Equilibrium shapes for droplets in shear flows with viscosity ratio $\lambda = 1$ and advancing contact angle $\theta_A = 90°$ for the y-constrained optimization problem. For (a–c) the capillary number is $Ca = 0, 0.02, 0.04, 0.06, 0.08, 0.09$. (a) The shape of the contact line. The small solid line shows the beginning of the jump region, while the dashed lines show the end of the region for different values of Ca. (b) The cross-section of the drop surface with the plane $y = 0$. (c) The variation of the contact angle θ as a function of the azimuthal angle ϕ. (d,e) The drop surface for capillary number $Ca = 0.09$.

free to move over a solid surface, these results show that the assumption of a circular contact line predicts a much smaller yield stress than would be achieved in practice.

Owing to the importance of wetted surface area in applications involving heat and mass transfer, we find it interesting to plot the ratio of the wetted area W to its initial value W_0 as a function of the capillary number Ca in figure 8 (c). The initial wetted area is given by $W_0 = \pi R^2 \sin^2 \theta_A$, where R is connected with the characteristic radius a via the relation $(4\pi/3)a^3 = V = (\pi/12)R^3(8 - 12\cos\theta_A + 4\cos^3\theta_A)$. With increasing capillary number, the wetted area of the unconstrained contact line is increased more than that of the y-constrained contact line while the circular contact line admits a higher area than the other two. This behaviour of the wetted area W is valid for all advancing contact angles θ_A as well as for all the viscosity ratios λ studied in this paper.

3.2. *Influence of the viscosity ratio λ*

Having considered the influence of the advancing contact angle θ_A on the displacement of a viscous drop with $\lambda = 1$, we now turn our attention to the effects of the viscosity ratio λ. We begin with the unconstrained optimization. Figure 9 (a,b) shows the
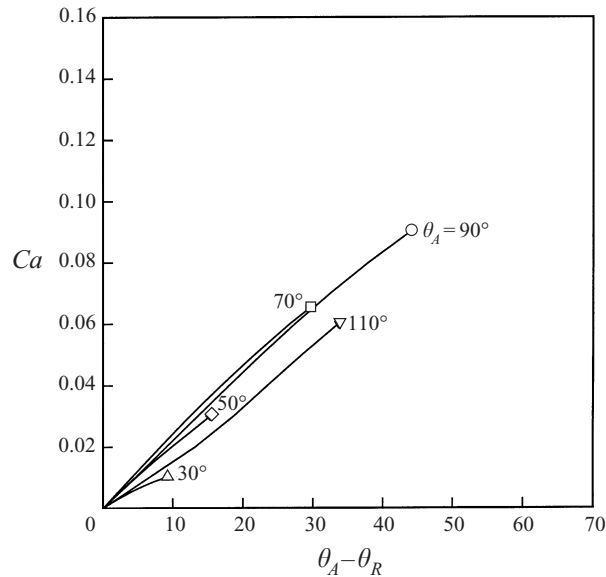
FIGURE 7. Critical capillary number Ca versus hysteresis $\theta_A - \theta_R$ for viscosity ratio $\lambda = 1$ and for the y-constrained optimization problem.

contact line contours and droplet profiles for a high-viscosity drop with viscosity ratio $\lambda = 10$, contact angle $\theta_A = 90°$ and for several values of the capillary number Ca. Comparing the unconstrained optimal contact lines for $\lambda = 1$ and $\lambda = 10$ at the same capillary number, we note that the high-viscosity drop shows greater extension in the y-direction. This is illustrated more clearly in figure 13 below, where we collect the contact lines for several viscosity ratios. The y-constrained contact lines for the more viscous drop (not shown) mimic the trends for the unconstrained case. For both the unconstrained and y-constrained cases, the high-viscosity droplets exhibit more deformation and greater hysteresis $\theta_A - \theta_R$ than the $\lambda = 1$ droplets at the same Ca. This behaviour may be anticipated from the force balance on the droplets. The more viscous drop experiences a greater hydrodynamic force, which must be balanced by an increased interfacial force. This increased surface force is achieved via a greater change in the contact angles on the front and rear portions of the contact line. The yield stress as a function of hysteresis for the $\lambda = 10$ droplets will be presented in figure 13 below.

Continuing our discussion of the viscosity effects, we consider the case of an inviscid droplet with $\lambda = 0$. Figure 10 (*a,b*) shows the contact line contours and droplet profiles for the unconstrained optimization of droplets with contact angle $\theta_A = 90°$. Three-dimensional views of the droplet for a typical Ca are shown in figure 10 (*c,d*). The corresponding curves for the y-constrained problem are plotted in figure 11 (*a–d*). The droplet behaviour illustrated in these figures is consistent with that observed for the viscous droplets above. Comparing the unconstrained contours for the cases $\lambda = 0$ and $\lambda = 1$, we see less deformation and lateral extension for the inviscid droplet. Similarly, for the y-constrained contours, the inviscid droplet shows less extension in the flow direction than that for the equivalent viscous droplet. As before, this behaviour is readily explained by the balance between the hydrodynamic and interfacial forces. The yield stress for the inviscid droplets is shown in figure 12 where we plot the critical Ca as a function of the hysteresis $\theta_A - \theta_R$ for $\lambda = 0$ and
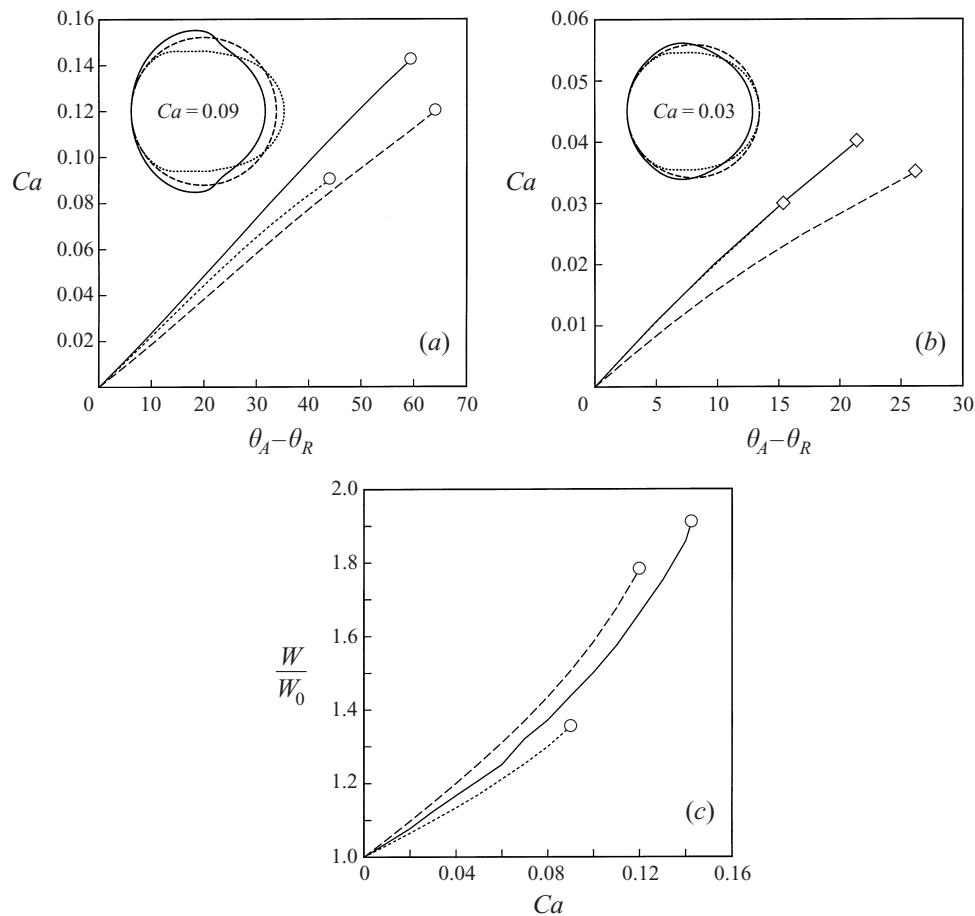
FIGURE 8. Influence of the shape of the contact line. (*a*) Critical capillary number *Ca* versus hysteresis $\theta_A - \theta_R$ for $\theta_A = 90°$, $\lambda = 1$ and for different optimal contact lines. (*b*) As in (*a*) but for $\theta_A = 50°$. (*c*) Ratio of the wetted area *W* to its initial value W_0 versus capillary number *Ca* for $\theta_A = 90°$, $\lambda = 1$ and for different optimal contact lines. Contact lines: ——, unconstrained; - - - -, *y*-constrained; – – – –, circular.

several values of θ_A. The results for an unconstrained contact line are shown in figure 12 (*a*) while figure 12 (*b*) shows the corresponding curves for a *y*-constrained contact line. These curves reveal that the influence of the advancing contact angle θ_A on an inviscid droplet is dramatically different from that for the viscous case. For an inviscid droplet ($\lambda = 0$) with specified hysteresis $\theta_A - \theta_R$, increasing θ_A *decreases* the critical shear rate. By contrast, increasing θ_A for a viscous drop *increases* the critical shear rate. This difference in the influence of θ_A for viscous and inviscid droplets is much more pronounced at the smaller contact angles θ_A.

The explanation for this curious phenomenon is straightforward when one considers the basic physics involved. For viscous droplets with small contact angles, the primary hydrodynamic force is the shear stress which is very close to $\tau_\infty \equiv \mu G$ independent of the internal viscosity. The hydrodynamic force is proportional to the surface area of the droplet and scales as $\tau_\infty r^2$, where r is the radius of the contact region. In terms of the characteristic drop radius a based on drop volume, this gives $\tau_\infty a^2 \theta_A^{-2/3}$. The interfacial force is proportional to the width of the contact region and scales as
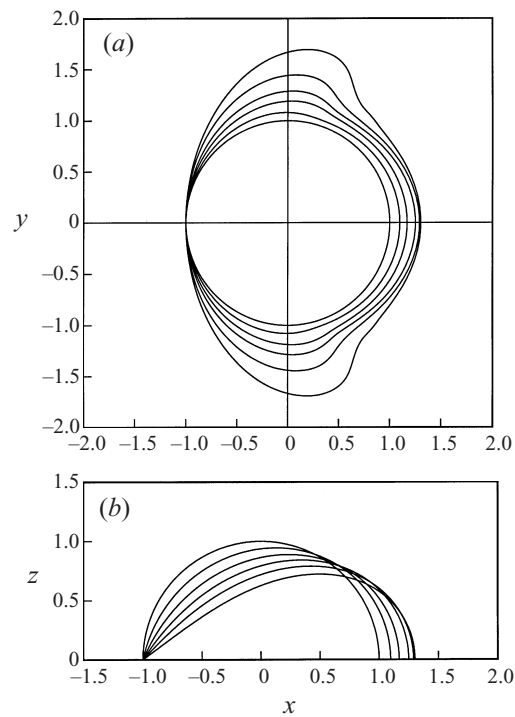
FIGURE 9. Equilibrium shapes for droplets in shear flows with viscosity ratio $\lambda = 10$ and advancing contact angle $\theta_A = 90°$, for the unconstrained optimization problem. (*a*) The shape of the contact line for $Ca = 0$, 0.02, 0.04, 0.06, 0.08, 0.10. (*b*) Drop profile for the same values of Ca as in (*a*).
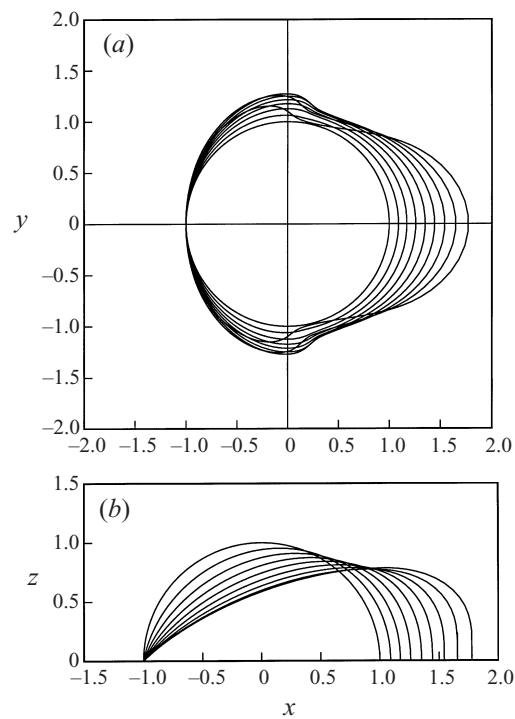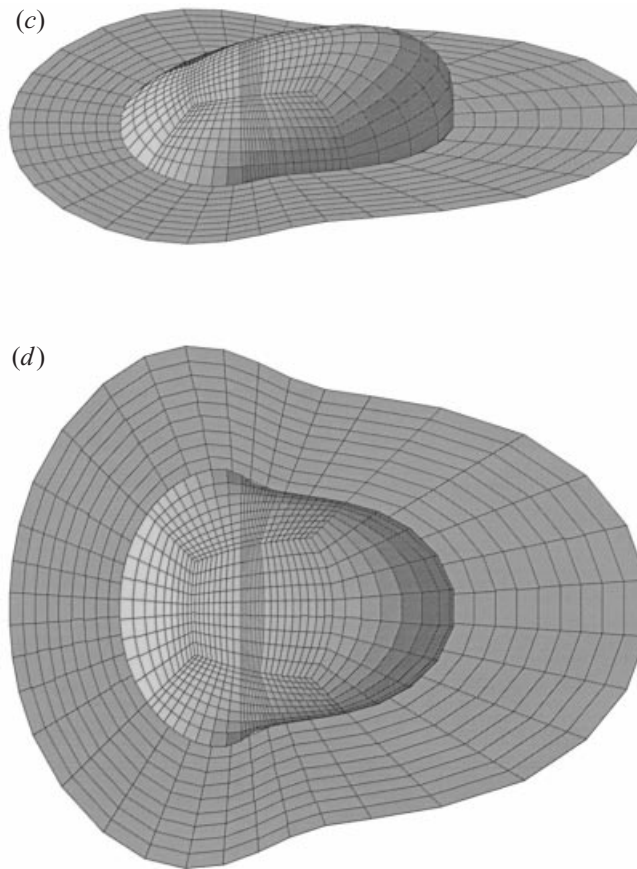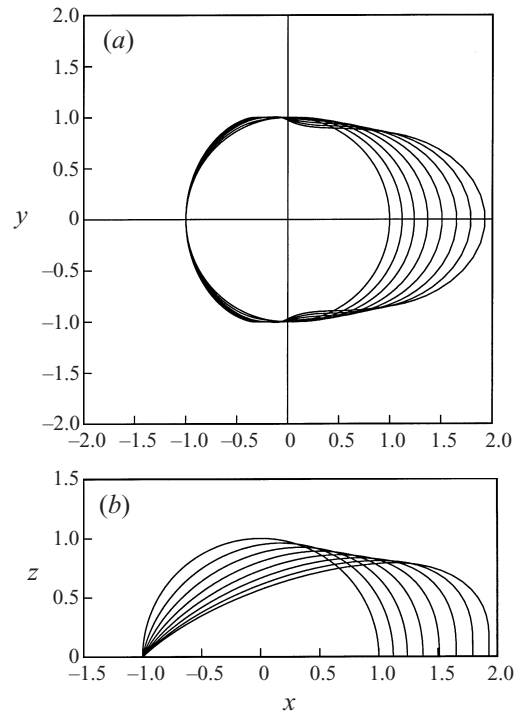

FIGURE 10 (*a*, *b*). For caption see facing page.

(*c*)

(*d*)

FIGURE 10. Equilibrium shapes for inviscid ($\lambda = 0$) droplets in shear flows with advancing contact angle $\theta_A = 90°$, for the unconstrained optimization problem. (*a*) The shape of the contact line for $Ca = 0$, 0.05, 0.10, 0.15, 0.20, 0.25, 0.30, 0.35, 0.36. (*b*) Drop profile for the same values of Ca as in (*a*). (*c,d*) The drop surface for capillary number $Ca = 0.36$.

$(\theta_A - \theta_R)\theta_A \gamma r \sim (\theta_A - \theta_R)\gamma a \theta_A^{2/3}$. As θ_A increases, the hydrodynamic force decreases, while the interfacial force increases. Thus a higher shear rate is required to dislodge the droplet when θ_A increases.

For the inviscid droplet, the shear stress is identically zero, and the hydrodynamic force is due to the pressure field. The pressure force on the inviscid droplet is insensitive to the contact area and is proportional to the frontal area of the drop. The pressure change over the droplet Δp is proportional to $\tau_\infty \theta_A$, and the total pressure force scales as $\tau_\infty \theta_A (\theta_A r^2)$ or $\tau_\infty a^2 \theta_A^{4/3}$. Increasing the contact angle θ_A increases the pressure force more rapidly than the surface force, hence a lower flow rate is sufficient to displace the droplet. Based on these phenomena one should be cautious in extrapolating results for a given viscosity ratio to droplets of different viscosities, e.g. in comparing liquid droplets and gas bubbles.

The physical arguments presented above also help to explain the difference in appearance between contact line contours for the viscous and inviscid droplets. The viscous droplets tend to spread out laterally, while the inviscid drops are elongated in the flow direction. The increased width for the viscous drop increases the surface force while the hydrodynamic shear force is insensitive to width for a given contact area.

P. Dimitrakopoulos and J. J. L. Higdon

FIGURE 11 (*a, b*). For caption see facing page.

Thus the viscous drop can increase its stability by spreading in the lateral direction. By contrast, for the inviscid drop, an increased width would significantly increase the pressure force offsetting any gain in surface force. Instead, the inviscid drops extends in the flow direction, because the pressure force is insensitive to the length of the droplet.

To illustrate more clearly the effect of viscosity ratio on the drop displacement process, we collect the results for several different viscosity ratios in figure 13. We plot the capillary number Ca as a function of the hysteresis $\theta_A - \theta_R$ for $\theta_A = 90°$ (figure 13 *a*) and for $\theta_A = 50°$ (figure 13 *b*). For brevity, we include only the results for the unconstrained contour lines. Note that the curves for an inviscid droplet ($\lambda = 0$) extend far above the top of the figures. These curves show that for large contact angles θ_A the high-viscosity droplets ($\lambda = 10$, $\lambda = 100$) show a significant departure from the $\lambda = 1$ results. On the other hand, for smaller angles θ_A this departure is significantly smaller. (Note that the two figures have different scales.) This trend is consistent with the predictions of the small-angle asymptotic theory of Dussan (1987). Clearly, the effects of the viscosity ratio should not be discounted for viscous fluids with $\lambda \geqslant 1$, and projections based on $\lambda = 1$ may give only qualitative predictions for more viscous fluids. In figure 13 (*a,b*), the inset contours show the unconstrained optimal contact lines for the different viscosity droplets for a typical capillary number, $Ca = 0.09$ ($\theta_A = 90°$) and $Ca = 0.025$ ($\theta_A = 50°$). In both figures, it is clear that the more viscous droplets show greater y-extension of the contact line. This effect is also manifested in a greater wetted surface area, as shown in figure 13 (*c*).

3.3. *Comparison with experimental results and asymptotic theory*

In this section, we briefly consider some experimental observations which may be compared qualitatively with the results of our computations. First, we note that there
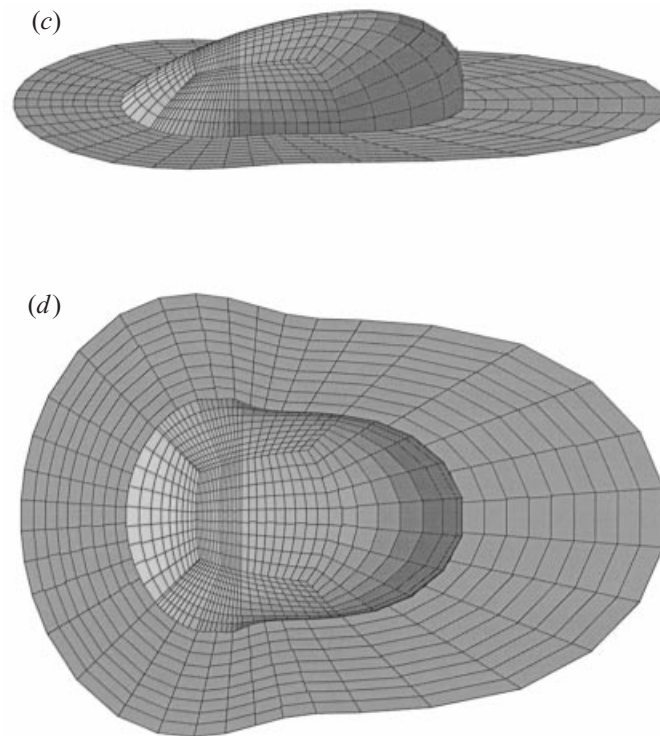
(*c*)

(*d*)

FIGURE 11. Equilibrium shapes for inviscid ($\lambda = 0$) droplets in shear flows with advancing contact angle $\theta_A = 90°$, for the *y*-constrained optimization problem. (*a*) The shape of the contact line for $Ca = 0$, 0.05, 0.10, 0.15, 0.20, 0.25, 0.30, 0.35. (*b*) Drop profile for the same values of Ca as in (*a*). (*c*,*d*) The drop surface for capillary number $Ca = 0.35$.

appear to be no detailed experimental results for the droplet shapes or yield stresses required for drop displacement in a viscous shear flow. The majority of experiments have focused on the displacement of droplets on inclined surfaces due to the action of gravity. Given these circumstances, we attempted some informal visualization studies for viscous displacement in a parallel plate geometry. These experiments were of limited extent and addressed only the qualitative issues concerning droplet shape. Figure 14 shows a typical result for a stationary air bubble attached to a Plexiglas substrate immersed in a flowing glycerol solution. This photograph may be compared with our predictions for the inviscid drops with unconstrained contours shown in figure 10 (*a,d*), and *y*-constrained results shown in figure 11 (*a,d*). Both predictions match the experiment in a number of key features including: elongation in the flow direction, asymmetry in the flow direction and in the indentation and inflection points on the sides of the bubble. While both predictions share these features, the *y*-constrained contours more closely resemble the experimental configuration. Recalling our earlier discussion, we note that the experimental procedure matched that described in conjunction with the *y*-constrained optimization. Specifically, the air bubble was injected via a syringe inserted through the wall of the substrate under quiescent conditions, and the contact line was observed to spread outward over the surface. The initial configuration of the bubble is thus approximately a sphere with contact angle θ_A. With this experiment, we would anticipate agreement with the *y*-constrained prediction.
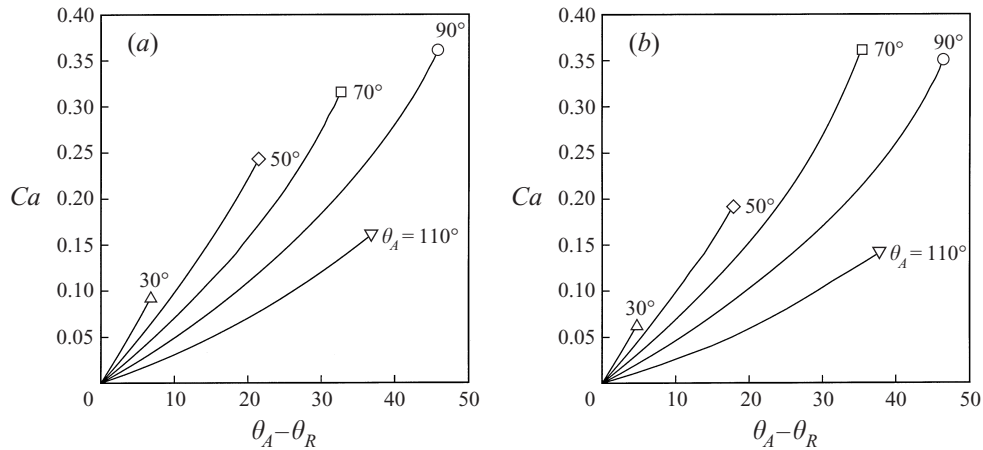
FIGURE 12. Critical capillary number *Ca* versus hysteresis $\theta_A - \theta_R$ for viscosity ratio $\lambda = 0$: (*a*) unconstrained contact line, (*b*) *y*-constrained contact line.

In contrast to the case for flowing systems, there have been a number of observations of droplet shape for drops on inclined surfaces. Early efforts (Bikerman 1950; Furmidge 1962) reported symmetric oval shapes with parallel sides for *sliding* droplets, but Bikerman sketched an asymmetric profile for the droplet at the instant of incipient motion. Rotenberg, Boruvka & Neumann (1984) also show asymmetric profiles for sliding drops. In a recent paper, Extrand & Kumagai (1995) observed the critical contact lines for droplets on inclined surfaces, and found curves which were neither circular, nor parallel sided, but exhibited asymmetric profiles consistent with the report of Bikerman. We emphasize that one should not expect an exact comparison between the results for the gravity and shear displacement problems, and we shall return to these results in our companion paper on the gravity problem (Dimitrakopoulos & Higdon 1998). The point of interest here is that many contours have been observed with fore-and-aft asymmetry and non-parallel sides. In contrast, previous theoretical and computational efforts have focused on symmetric contours with circular, elliptical or oval planforms.

The prediction of the yield stress for droplet displacement is probably the most important issue addressed in this paper. Unfortunately, there are no experimental results with which we may make direct comparison. On the computational side, Li & Pozrikidis (1996) studied the three-dimensional displacement problem for contact lines with fixed elliptical shape. These authors limited their computations to a small set of parameter values and did not provide predictions for the yield condition. We have checked their results for contact angles and droplet shapes and find excellent agreement with our predictions.

The sole reference for quantitative predictions for the critical *Ca* in the viscous displacement problem is the asymptotic theory of Dussan (1987). Dussan assumed a droplet contour with an oval shape with parallel sides. She further assumed a constant angle θ_R on the front portion of the oval and a constant angle θ_A on the rear. With these assumptions, she employed lubrication theory to find the size of the contact region and the yield condition. Dussan's theory is valid in the joint asymptotic limits $\theta_A - \theta_R \ll \theta_A \ll 1$. The assumptions made by Dussan (see Dussan & Chow 1983 for detailed justification) are broadly consistent with the results of our *y*-constrained optimization solutions for viscous drops. Moreover, for small contact angles θ_A, we
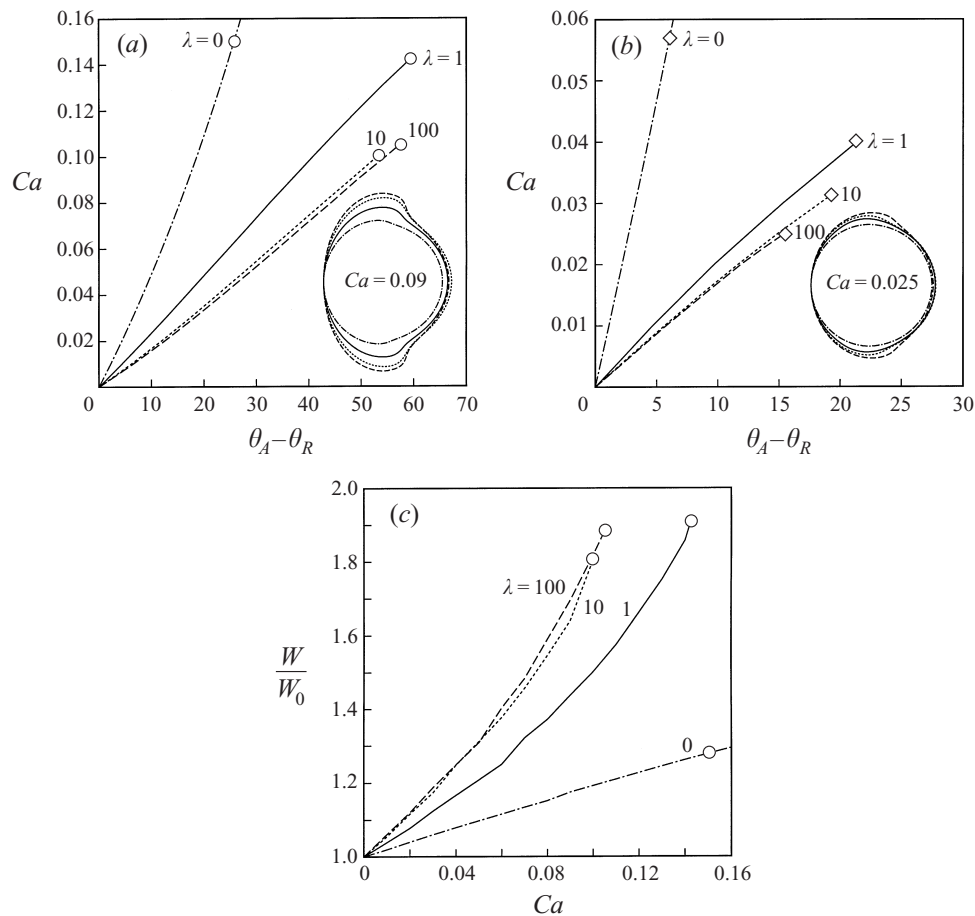
FIGURE 13. Influence of the viscosity ratio for unconstrained optimal contact lines. (*a*) Critical capillary number *Ca* versus hysteresis $\theta_A - \theta_R$ for $\theta_A = 90°$ and for several viscosity ratios. (*b*) As in (*a*) but for $\theta_A = 50°$. (*c*) Ratio of the wetted area W to its initial value W_0 versus capillary number *Ca* for $\theta_A = 90°$ and for several viscosity ratios.

have seen that the predictions for the yield stress for unconstrained optimization are quite close to those for the *y*-constrained case, even though the contact line contours differ dramatically. Given these circumstances, we should expect reasonable agreement with Dussan's results in the appropriate asymptotic limits. A direct comparison of our results with Dussan's theory is not possible, because our numerical computations are limited to advancing contact angles $\theta_A \geqslant 30°$, while Dussan's theory is valid as $\theta_A \to 0$. To make a direct comparison, we must employ our results for several contact angles and extrapolate to the asymptotic regime.

In the asymptotic limits $\theta_A - \theta_R \ll \theta_A \ll 1$, Dussan gives the critical capillary number for viscous droplets in the form

$$Ca_{asym} = 0.2804\, \theta_A^{4/3} \,(\theta_A - \theta_R). \tag{30}$$

Thus the asymptotic theory predicts that the critical capillary number is independent of the viscosity ratio λ. In our results, we have seen previously that the effect of viscosity ratio diminishes for small contact angles, and thus we find agreement with this aspect of the asymptotic theory.
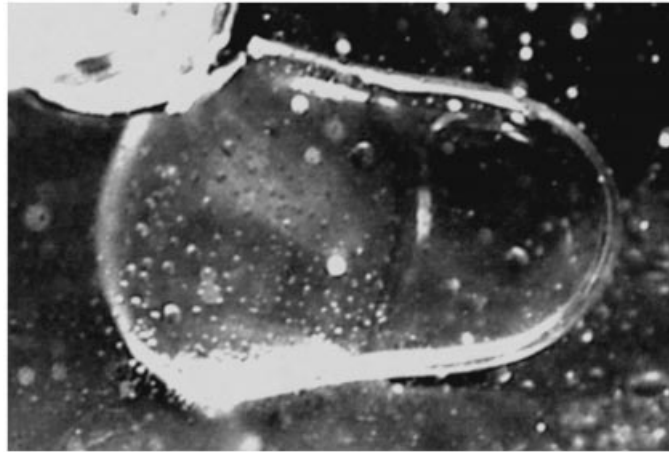
FIGURE 14. A stationary air bubble attached to a Plexiglas substrate immersed in a flowing glycerol solution.
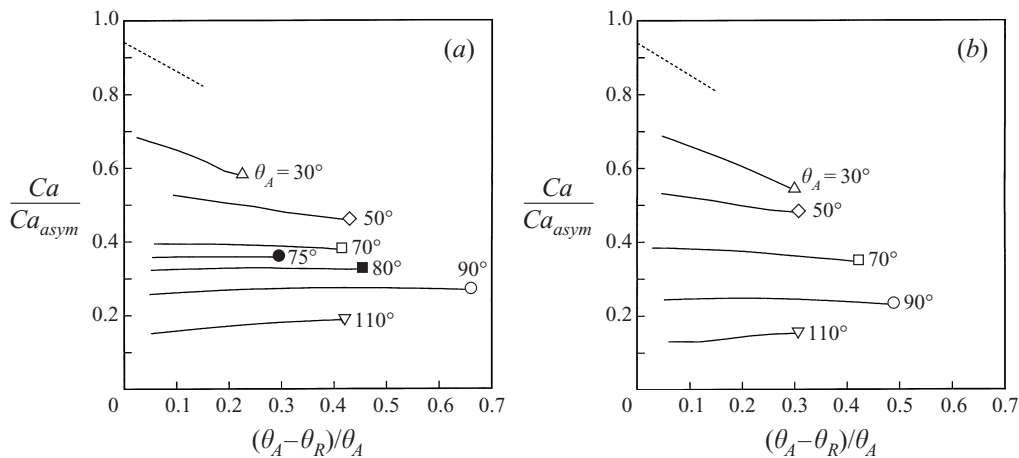

FIGURE 15. Ratio of critical *Ca* to asymptotic predictions based on (30) for viscosity ratio $\lambda = 1$. (*a*) Unconstrained optimal contact line. (*b*) *y*-constrained contact line.

To test the validity of our computations, and to assess the practical limits on the application of the asymptotic theory, we consider the ratio of our computed *Ca* with the asymptotic prediction. This quantity is plotted in figure 15 as a function of the reduced hysteresis $(\theta_A - \theta_R)/\theta_A$. The individual solid curves correspond to computations for different values of the advancing contact angle θ_A. Based on these results, we conclude that the quantitative predictions of the asymptotic theory are valid over a very limited range, with poor agreement with all direct numerical results of this paper. In fact, this is not surprising since Dussan's theory requires not only $\theta_A \ll 1$, but also $\theta_A - \theta_R \ll \theta_A$. Thus the theory is valid only for vanishingly small values of the contact angle hysteresis, i.e. only within a very small region in the upper left corner of figure 15. Even in the limit as $\theta_A - \theta_R \to 0$, the predictions shown on figure 15 for finite θ_A show significant error as indicated by the intercepts of the curves with the ordinate axis.

Despite its limited predictive range, the asymptotic lubrication theory is of significant interest, because it captures the correct physics and provides the proper scaling for small contact angles. Furthermore, it provides a rigorous check on the overall validity of our computations. To pursue this comparison, we extrapolated our results in the dual limits $\theta_A \to 0$ and $(\theta_A - \theta_R)/\theta_A \to 0$ and have plotted the results as the dashed lines in figure 15. These extrapolations show good agreement with Dussan's theory with the ratio of numerical results/asymptotic prediction $= 94\%$. This slight departure may be attributed to the different assumptions regarding the contact line contours and to the uncertainty involved in a rather large extrapolation from our minimum contact angle of $\theta_A = 30°$.

As a final point, we note that the lubrication theory employed by Dussan is valid only for viscous fluids, and that the limit $\lambda \to 0$ is a singular limit. For droplets whose viscosity ratio is $\lambda \ll \theta_A$, the force balance between pressure and interfacial forces (presented earlier in reference to figure 12) yields a new scaling for the critical capillary number

$$Ca_{asym} \sim \theta_A^{-2/3} (\theta_A - \theta_R). \tag{31}$$

This asymptotic behaviour for low-viscosity droplets is analogous to that reported for two-dimensional droplets in our earlier study (DH).

4. Conclusions

In this paper we have conducted a comprehensive study of the drop displacement problem for three-dimensional droplets in viscous shear flows. We have considered a wide selection of parameters to investigate the physical behaviour of different droplets and to test the limits of theoretical predictions. This study complements the analytical theory of Dussan (1987) for displacement of droplets in low Reynolds number flows. A number of important conclusions have been reached.

(i) The contact line contours for real droplets show fore-and-aft asymmetry with a distorted shape not well represented by the simple circle/elliptical planforms assumed by previous authors. The distorted profiles allow sharp jumps in contact angle which increases the ability of a droplet to stick to a surface. The contact line contours predicted by our simulations show good qualitative agreement with experimental observations.

(ii) The yield stress predicted by the unconstrained optimization provides an upper bound on the yield condition for a droplet on a solid substrate. Alternative droplet configurations resulting from the y-constrained optimization show only a small change in the predicted yield stress compared to the unconstrained case. Predictions based on circular contact lines show a significant change in the critical yield stress.

(iii) Asymptotic results based on lubrication theory should give correct qualitative predictions for the behaviour of *viscous* drops; however the range of validity is quite small, and the quantitative predictions show significant errors. The critical capillary number shows significant departure from the linear dependence on hysteresis $\theta_A - \theta_R$ predicted by asymptotic theories.

(iv) Viscosity ratio plays an important role for viscous droplets, showing a significant effect at high contact angles. This sensitivity to viscosity ratio is not predicted by lubrication theory.

(v) Inviscid droplets show dramatic and often contradictory behaviour compared to viscous droplets. These effects are most severe at small contact angles. Gas bubbles

220   *P. Dimitrakopoulos and J. J. L. Higdon*

and liquid droplets may be expected to show dramatically different behaviour owing to these differences.

We close by noting that the three-dimensional Newton iteration procedure introduced in this paper proved to be a robust and efficient numerical technique. We believe it will prove well suited to study other equilibrium problems in low-Reynolds-number flows.

Appendix

In this Appendix we present the explicit form of the functions $n'(d)$ and $\nabla \cdot n$. To calculate the unit normal vector $n \equiv x_\xi \times x_\eta / |x_\xi \times x_\eta|$ on Γ, we first calculate the surface derivatives x_ξ and x_η on Γ by differentiating (12), which leads to

$$x_\xi = x_\xi^0 + p_\xi\, d + p\, d_\xi, \tag{A1}$$

$$x_\eta = x_\eta^0 + p_\eta\, d + p\, d_\eta, \tag{A2}$$

where the subscripts ξ and η denote the surface derivatives $\partial/\partial\xi$ and $\partial/\partial\eta$ respectively. In this section, any geometric variable with a superscript (or subscript) 0 is calculated on the interface Γ_0, while the remaining variables are calculated on the interface Γ. Exceptions are the prescribed vector p and its derivatives, which are defined only on the interface Γ_0 and thus the superscript (or subscript) 0 is omitted.

In deriving the expressions for the unit normal vector n, it proves convenient to introduce the vector $v = x_\xi \times x_\eta$, which is a normal vector of non-unit magnitude. The vector v on Γ is connected with the normal vector $v_0 = x_\xi^0 \times x_\eta^0$ on Γ_0 by

$$v = v_0 + v'(d) + O(d^2), \tag{A3a}$$

where

$$v'(d) = (x_\xi^0 \times p_\eta + p_\xi \times x_\eta^0)\, d + (p \times x_\eta^0)\, d_\xi + (x_\xi^0 \times p)\, d_\eta. \tag{A3b}$$

The magnitude ω of the normal vector v on Γ is given by

$$\omega \equiv |x_\xi \times x_\eta| = \omega_0 + \frac{v_0 \cdot v'}{\omega_0} + O(d^2), \tag{A4}$$

where $\omega_0 = |x_\xi^0 \times x_\eta^0|$ is the magnitude of the normal vector v_0 on Γ_0.

The unit normal vector $n = v/\omega$ on Γ is then

$$n = n_0 + \left[\frac{v'}{\omega_0} - \frac{v_0 \cdot v'}{\omega_0^2}\, n_0\right] + O(d^2), \tag{A5}$$

where the second term on the right-hand side of this equation is the function $n'(d)$.

The curvature $\nabla \cdot n$ on Γ is given by

$$\nabla \cdot n = \frac{2\,(x_\xi \cdot x_\eta)(x_{\xi\eta} \cdot v) - (x_\eta \cdot x_\eta)(x_{\xi\xi} \cdot v) - (x_\xi \cdot x_\xi)(x_{\eta\eta} \cdot v)}{\omega^3}. \tag{A6}$$

The surface derivatives $x_{\xi\xi}$, $x_{\xi\eta}$ and $x_{\eta\eta}$ on Γ are calculated by differentiating (A1)

and (A 2)

$$\boldsymbol{x}_{\xi\xi} = \boldsymbol{x}^0_{\xi\xi} + \boldsymbol{p}_{\xi\xi}\, d + 2\,\boldsymbol{p}_\xi\, d_\xi + \boldsymbol{p}\, d_{\xi\xi}, \tag{A 7}$$

$$\boldsymbol{x}_{\xi\eta} = \boldsymbol{x}^0_{\xi\eta} + \boldsymbol{p}_{\xi\eta}\, d + \boldsymbol{p}_\eta\, d_\xi + \boldsymbol{p}_\xi\, d_\eta + \boldsymbol{p}\, d_{\xi\eta}, \tag{A 8}$$

$$\boldsymbol{x}_{\eta\eta} = \boldsymbol{x}^0_{\eta\eta} + \boldsymbol{p}_{\eta\eta}\, d + 2\,\boldsymbol{p}_\eta\, d_\eta + \boldsymbol{p}\, d_{\eta\eta}. \tag{A 9}$$

After some algebra, the numerator of (A 6) obtains the form $A_0 + A'(d) + O(d^2)$, i.e. is expressed, with an error of $O(d^2)$, in terms of the corresponding variable A_0 on Γ_0 and known functions and derivatives of d, $A'(d)$. The explicit expression for $A'(d)$ is omitted, but is readily obtainable by substitution in (A 6) using equations (A 1)–(A 4) and (A 7)–(A 9).

The curvature $\nabla \cdot \boldsymbol{n}$ on Γ is then given by

$$\nabla \cdot \boldsymbol{n} = \nabla \cdot \boldsymbol{n}_0 + \left[\frac{A'(d)}{\omega_0^3} - 3\,(\nabla \cdot \boldsymbol{n}_0)\,\omega_0\,(\boldsymbol{v}_0 \cdot \boldsymbol{v}') \right] + O(d^2). \tag{A 10}$$

Combining (A 5) and (A 10), the curvature term $(\nabla \cdot \boldsymbol{n})\boldsymbol{n}$, which is used in (19), is expressed easily in terms of its unperturbed value on Γ_0 and functions and derivatives of d.

REFERENCES

BARTHÈS-BIESEL, D. & ACRIVOS, A. 1973 Deformation and burst of a liquid droplet freely suspended in a linear shear field. *J. Fluid Mech.* **61**, 1–21.

BIEGLER, L. T., COLEMAN, T. F., CONN, A. R. & SANTOSA, F. N. 1997 *Large-Scale Optimization with Applications. Part II: Optimal Design and Control.* Springer.

BIKERMAN, J. J. 1950 Sliding of drops from surfaces of different roughnesses. *J. Colloid Sci.* **5**, 349–358.

BROWN, R. A., ORR, F. M. JR & SCRIVEN, L. E. 1980 Static drop on an inclined plate: analysis by the finite element method. *J. Colloid Interface Sci.* **73**, 76–87.

CANUTO, C., HUSSAINI, M. Y., QUARTERONI, A. & ZANG, T. A. 1988 *Spectral Methods in Fluid Dynamics.* Springer.

CHEN, Q., RAME, E. & GAROFF, S. 1995 The breakdown of asymptotic hydrodynamic models of liquid spreading at increasing capillary number. *Phys. Fluids* **7**, 2631–2639.

CHRISTODOULOU, K. N. & SCRIVEN, L. E. 1992 Discretization of free surface flows and other moving boundary problems. *J. Comput. Phys.* **99**, 39–55.

DIMITRAKOPOULOS, P. & HIGDON, J. J. L. 1997 Displacement of fluid droplets from solid surfaces in low-Reynolds-number shear flows. *J. Fluid Mech.* **336**, 351–378 (referred to herein as DH).

DIMITRAKOPOULOS, P. & HIGDON, J. J. L. 1998 On the gravitational displacement of three-dimensional fluid droplets from inclined solid surfaces. To be submitted to *J. Fluid Mech.*

DUSSAN V., E. B. 1979 On the spreading of liquids on solid surfaces: static and dynamic contact lines. *Ann. Rev. Fluid Mech.* **11**, 371–400.

DUSSAN V., E. B. 1985 On the ability of drops or bubbles to stick to non-horizontal surfaces of solids. Part 2. Small drops or bubbles having contact angles of arbitrary size. *J. Fluid Mech.* **151**, 1–20.

DUSSAN V., E. B. 1987 On the ability of drops to stick to surfaces of solids. Part 3. The influences of the motion of the surrounding fluid on dislodging drops. *J. Fluid Mech.* **174**, 381–397.

DUSSAN V., E. B. & CHOW, R. T.-P. 1983 On the ability of drops or bubbles to stick to non-horizontal surfaces of solids. *J. Fluid Mech.* **137**, 1–29.

EXTRAND, C. W. & KUMAGAI, Y. 1995 Liquid drops on an inclined plane: the relation between contact angles, drop shape, and retentive force. *J. Colloid Interface Sci.* **170**, 515–521.

FENG, J. Q. & BASARAN, O. A. 1994 Shear flow over a translationally symmetric cylindrical bubble pinned on a slot in a plane wall. *J. Fluid Mech.* **275**, 351–378.

FURMIDGE, C. G. L. 1962 Studies at phase interfaces: the sliding of liquid drops on solid surfaces and a theory for spray retention. *J. Colloid Sci.* **17**, 309–324.

HIGDON, J. J. L. & SCHNEPPER, C. A. 1994 High order boundary integral methods for viscous free surface flows. In *Free Boundaries in Viscous Flows* (ed. R. A. Brown & S. H. Davis). Springer.

KISTLER, S. F. 1993 Hydrodynamic wetting. In *Wettability* (ed. J. C. Berg). Dekker.

KISTLER, S. F. & SCRIVEN, L. E. 1984*a* Coating flow theory by finite element and asymptotic analysis of the Navier-Stokes system. *Intl J. Numer. Meth. Fluids* **4**, 207–229.

KISTLER, S. F. & SCRIVEN, L. E. 1984*b* Coating flows. In *Computational Analysis of Polymer Processing* (ed. J. R. A. Pearson & S. M. Richardson). Applied Science Publishers.

LI, X. & POZRIKIDIS, C. 1996 Shear flow over a liquid drop adhering to a solid surface. *J. Fluid Mech.* **307**, 167–190.

MILINAZZO, F. & SHINBROT, M. 1988 A numerical study of a drop on a vertical wall. *J. Colloid Interface Sci.* **121**, 254–264.

MULDOWNEY, G. P. & HIGDON, J. J. L. 1995 A spectral boundary element approach to three-dimensional Stokes flow. *J. Fluid Mech.* **298**, 167–192.

OCCHIALINI, J. M., MULDOWNEY, G. P. & HIGDON, J. J. L. 1992 Boundary integral/spectral element approaches to the Navier-Stokes equations. *Intl J. Num. Meth. Fluids* **15**, 1361–1381.

OLIVER, J. F., HUH, C. & MASON, S. G. 1977 Resistance to spreading of liquids by sharp edges. *J. Colloid Interface Sci.* **59**, 568–581.

POZRIKIDIS, C. 1992 *Boundary Integral and Singularity Methods for Linearized Viscous Flow*. Cambridge University Press.

ROTENBERG Y., BORUVKA, L. & NEUMANN, A. W. 1984 The shape of nonaxisymmetric drops on inclined planar surfaces. *J. Colloid Interface Sci.* **102**, 424–434.

SAITO, H. & SCRIVEN, L. E. 1981 Study of coating flow by the finite element method. *J. Comput. Phys.* **42**, 53–76.